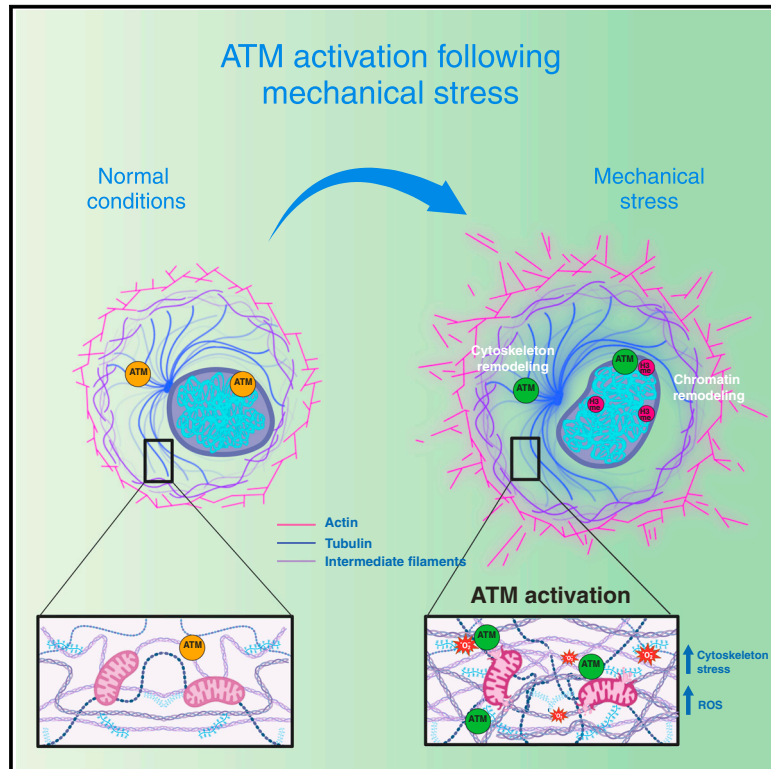# Cell stretching activates an ATM mechano-transduction pathway that remodels cytoskeleton and chromatin

Graphical abstract

Authors

Giulia Bastianello, Giancarlo Porcella, Galina V. Beznoussenko, ..., Vincenzo Costanzo, Giorgio Scita, Marco Foiani

Correspondence

giulia.bastianello@ifom.eu (G.B.), marco.foiani@ifom.eu (M.F.)

In brief

Cells adapt to mechanical forces by activating specific mechano-transduction pathways that control chromatin organization, nuclear integrity, and cytoskeleton properties. Bastianello et al. show that the ATM kinase, also involved in the DNA damage response, is activated by mechanical stress through a ROS-dependent mechanism and promotes cytoskeleton and chromatin remodeling.

Highlights

- ATM kinase is activated by mechanical stress

- ATM binds to cytoskeleton and controls cell stiffness and migration

- ATM promotes Kap1 S473 phosphorylation following cell stretching

- ATM defects compromise chromatin remodeling in response to mechanical stress

CellPress

Cell Reports

Article

Cell stretching activates an ATM mechano-transduction pathway that remodels cytoskeleton and chromatin

Giulia Bastianello,[1,2,*] Giancarlo Porcella,[1] Galina V. Beznoussenko,[1] Gururaj Kidiyoor,[1] Flora Ascione,[1] Qingsen Li,[1]
Angela Cattaneo,[3] Vittoria Matafora,[1] Andrea Disanza,[1] Micaela Quarto,[1] Alexander A. Mironov,[1] Amanda Oldani,[1]
Sara Barozzi,[1] Angela Bachi,[1] Vincenzo Costanzo,[1,2] Giorgio Scita,[1,2] and Marco Foiani[1,2,4,5,*]
[1]IFOM, the FIRC Institute of Molecular Oncology, 20139 Milan, Italy
[2]Oncology and Haemato-Oncology Department, University of Milan, 20122 Milan, Italy
[3]Cogentech SRL Benefit Corporation, 20139 Milan, Italy
[4]Present address: Cancer Science Institute of Singapore, National University of Singapore, Singapore, Singapore
[5]Lead contact
*Correspondence: giulia.bastianello@ifom.eu (G.B.), marco.foiani@ifom.eu (M.F.)
https://doi.org/10.1016/j.celrep.2023.113555

SUMMARY

Ataxia telangiectasia mutated (ATM) and ataxia telangiectasia and Rad3-related (ATR) DNA damage response (DDR) kinases contain elastic domains. ATM also responds to reactive oxygen species (ROS) and ATR to nuclear mechanical stress. Mre11 mediates ATM activation following DNA damage; ATM mutations cause ataxia telangiectasia (A-T). Here, using in vivo imaging, electron microscopy, proteomic, and mechano-biology approaches, we study how ATM responds to mechanical stress. We report that cytoskeleton and ROS, but not Mre11, mediate ATM activation following cell deformation. ATM deficiency causes hyper-stiffness, stress fiber accumulation, Yes-associated protein (YAP) nuclear enrichment, plasma and nuclear membrane alterations during interstitial migration, and H3 hyper-methylation. ATM locates to the actin cytoskeleton and, following cytoskeleton stress, promotes phosphorylation of key cytoskeleton and chromatin regulators. Our data contribute to explain some clinical features of patients with A-T and pinpoint the existence of an integrated mechano-response in which ATM and ATR have distinct roles unrelated to their canonical DDR functions.

INTRODUCTION

Ataxia telangiectasia mutated (ATM) is implicated in DNA double-strand break (DSB) repair.[1,2] ATM mutations cause the neurodegenerative disorder ataxia telangiectasia (A-T), characterized by the progressive degeneration of Purkinje cells leading to cerebellar ataxia. Additional features include telangiectasia, immunodeficiency, ionizing radiation sensitivity, cancer predisposition, and diabetes.[3] ATM phosphorylates several proteins involved in non-nuclear pathways[4–6] and localizes, in part, at neuronal presynaptic vesicles, mitochondria, and peroxisomes.[7–11] ATM can be activated in response to oxidative stress[12,13] and also regulates interleukin-8 (IL-8) to sustain cell migration.[14]

ATM shares similarities to ATR (ataxia telangiectasia and Rad3 related) and mTOR (mechanistic target of rapamycin).[15] The N termini of these proteins contain HEAT (Hungtinton, Elongation Factor 3, PR65/A, TOR) repeats that exhibit elastic properties.[16,17] Both ATR and mTOR respond to mechanical stress.[18–20] ATR is activated by mechanical stress following nuclear deformations and preserves nuclear envelope (NE) integrity.[21]

Mechanical forces govern chromosome function[22]; cells experience mechanical stress under many circumstances and

survive by activating mechano-transduction pathways influencing cancer, aging, and neurodegenerative diseases.[23–26] Human tissues exhibit a wide range of stiffness, and matrix stiffness determines cell fate during differentiation[27]; skeletal and muscles cells are constantly subjected to mechanical deformations, and migrating immune cells and metastatic cancer cells need to squeeze their nuclei while circulating and migrating across small constrictions[28–30] and microenvironments with different degrees of stiffness.[31]

The nucleus, being the stiffest organelle, is the key player in transmission of extracellular and intracellular mechanical forces.[32] Mechanical perturbations of the cytoskeleton affect nuclear plasticity, and the mechanical properties of cytoskeleton and nucleus can influence NE dynamics, chromatin organization, genome integrity, and cell migration.[28–30,33–36] The nucleus acts as a size sensor under compression to regulate cytoskeletal dynamics.[37,38]

Here, we show that ATM is activated by cell stretching and compression generated during interstitial migration. Part of ATM interacts with the cytoskeleton, phosphorylates chromatin and cytoskeleton proteins following cell stretching, and promotes cell survival during interstitial migration. Hence, ATM, like ATR, is activated by mechanical stress. However, while
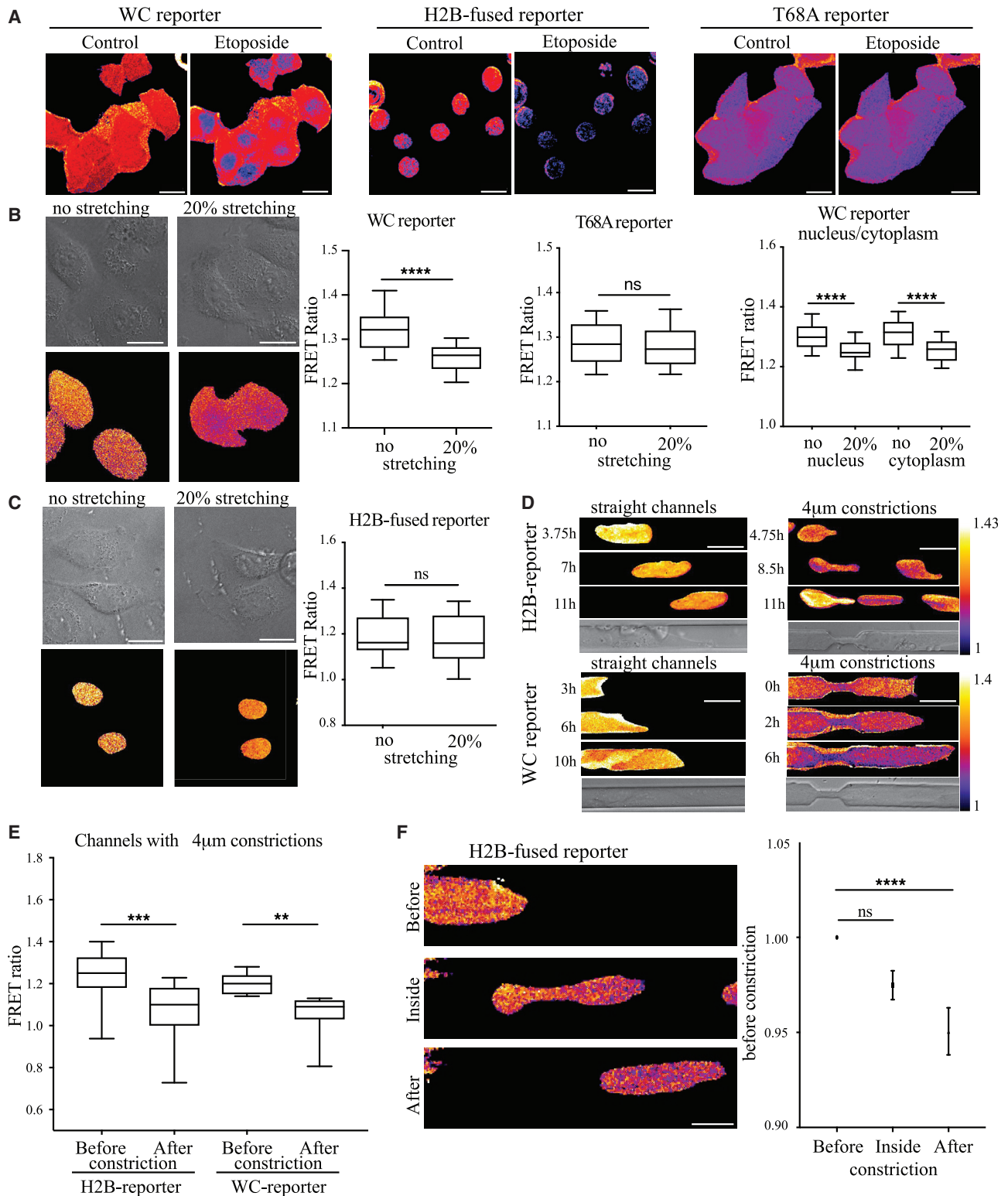
Figure 1. ATM is activated by mechanical stress during cell stretching and interstitial migration

(A) ATM activation was measured by FRET signal in HeLa cells expressing the WC or H2B-fused reporters following treatment with 30 μg/mL etoposide for 1 h (scale bars, 20 μm).

(legend continued on next page)

ATR controls the mechanical properties of the nucleus, ATM mediates a mechano-transduction pathway, regulating chromatin and cytoskeleton remodeling.

RESULTS

Cell stretching and interstitial migration activate ATM

We tested whether mechanical stress activates ATM using an ATM-FRET (fluorescence resonance energy transfer) reporter system[39] (Figure S1A). The reporter can be expressed in the whole cell (WC reporter) or in the nucleus (H2B-fused reporter). Following phosphorylation by ATM, the reporter undergoes conformational changes resulting in a decrease of the FRET signal, providing a readout of ATM activation. We also used a control FRET reporter that cannot be phosphorylated by ATM due to a mutation on threonine 68 (T68A reporter) (Figure S1A). We monitored ATM activation in HeLa cells in response to DNA damage induced by etoposide, a radiomimetic drug[40] (Figure 1A). Etoposide treatment activated the WC and the H2B-fused reporters but not the T68A reporter (Figure 1A). To investigate whether mechanical stress activates ATM, we developed a cell-stretching device that induces uni-axial stretching in a controlled manner.[41] Although 20% cell stretching did not cause DNA damage, as measured by pS139-γH2AX or 53BP1 foci accumulation (Figure S1B), the WC reporter was activated at comparable levels in the cytoplasm and the nucleus (Figure 1B). The T68A reporter and the H2B-fused reporter remained inactive (Figures 1B and 1C). We obtained analogous results in U2OS cells (Figure S1C). 20% stretching caused a rapid nuclear expansion, which recovered by 30 min (Figure S1D). Hence, following uni-axial cell stretching, nuclear and cytoplasmic ATM, but not chromatin-bound ATM, is activated through a process that does not correlate with DNA damage.

Interstitial migration causes mechanical stress as cells undergo cytoskeleton and nuclear deformation.[42] We used microchannel devices without and with constrictions[34,43] to measure ATM activation in U2OS cells (Figure 1D). We observed activation of ATM using the WC and the H2B-fused reporters specifically in channels with constrictions (Figures 1D, 1E, and S1E). We also found active chromatin-bound ATM within a longitudinal nuclear area (Figure 1D) where the nucleus undergoes cytoskeleton-mediated invaginations.[30] We monitored ATM activation using the H2B-fused reporter in cells passing across constrictions by analyzing three events (Figure 1F): (1) cells approaching the pores, (2) cells inside the constrictions, and (3) cells passed through the pores. ATM activation began while the nuclei were engaged into the constrictions and increased until the nuclei passed the pores (Figure 1F). We note that confined migration through constrictions with a limiting pore size generates DNA damage due to NE ruptures and leakage of DNA repair factors out of the nucleus.[44] In our devices, we used 4×6 μm pore size for U2OS cells to prevent DNA damage formation when cells engage the constrictions.[21,34] Hence, ATM can be activated by mechanical stress such as cell stretching, which causes cytoskeleton stress and transient nuclear expansion, and during interstitial migration, which leads to prolonged cell compression and nuclear deformation. The specific activation of the H2B-fused FRET reporter during interstitial migration can be due to the different mechanical stress generated at the nuclear level when cells migrate across pores; while during cell stretching, the cells respond to an immediate external mechanical stimulus and can modulate the mechanical stress at the nuclear level by cytoskeleton remodeling and nuclear orientation,[45,46] during interstitial migration, the nucleus is forced to deform at greater extents and for longer times.[47]

Mechanical stress-induced ATM activation does not depend on Mre11 but is influenced by cytoskeleton and reactive oxygen species (ROS)

WC reporter activation following cell stretching was abolished in the presence of the ATM catalytic inhibitor KU-60019 (Figure 2A). We then investigated the role of Mre11, a key factor mediating ATM activation at DSBs.[48] Mre11 was not required for ATM activation following cell stretching (Figure 2B). Cell stretching generates mechanical forces that are transduced by the cytoskeleton that links the plasma membrane to the NE.[49] We addressed the contribution of the actin cytoskeleton to ATM activation upon 20% stretching by treating cells with Rock inhibitors or Blebbistatin, which both impair actomyosin contractility through distinct mechanisms[50,51] (Figure 2C). Both treatments abolished ATM activation. ATM is a redox sensor and was shown to respond to ROS in the absence of DNA damage.[13] Since ROS increase following mechanical stress as a consequence of cytoskeletal-induced mitochondrial ruptures,[52] we addressed the contribution of ROS in ATM activation upon cell stretching by treating cells with the N-acetyl-cysteine (NAC) ROS scavenger (Figure 2D). NAC treatment abolished ATM activation. We then addressed whether pharmacologically induced cytoskeleton stress resulted in ATM activation (Figure 2E). Treatment with jasplakinolide, which stabilizes actin stress fibers, increased ATM-S1981 phosphorylation (a readout of ATM activation[53]) but did not cause γH2AX phosphorylation (Figure 2E).

ATM preserves the mechanical properties of the cell

Based on the previous results, ATM deficiency should influence the mechanical properties of the cell. We therefore measured cell stiffness by atomic force microscopy (AFM)[54–57] in ATM-deficient HeLa cells. ATM inhibition or depletion increased cell

(B) HeLa cells expressing the WC or T68A reporters were subjected to 20% uni-axial stretching. The signals were analyzed in cytoplasmic and nuclear compartments (scale bars, 20 μm). ****p < 0.0001, two-tailed t test. ****p < 0.0001, one-way ANOVA test.

(C) HeLa cells expressing chromatin-bound H2B reporter were analyzed (scale bars, 20 μm).

(D) U2OS cells expressing the H2B-fused or WC reporters were analyzed during migration into channels with or without constrictions at different time points (scale bars, 20 μm).

(E) Quantifications of average FRET signals of WC and H2B-fused reporters in cells before and after constrictions. ***p < 0.001, **p < 0.01, one-way ANOVA test.

(F) Representative images showing ATM activation during the passage of nuclei across pores and quantifications of the FRET signals before, during, and after the passage through the constrictions (scale bar, 10 μm). ****p < 0.0001, one-way ANOVA test; error bars represent SEM.
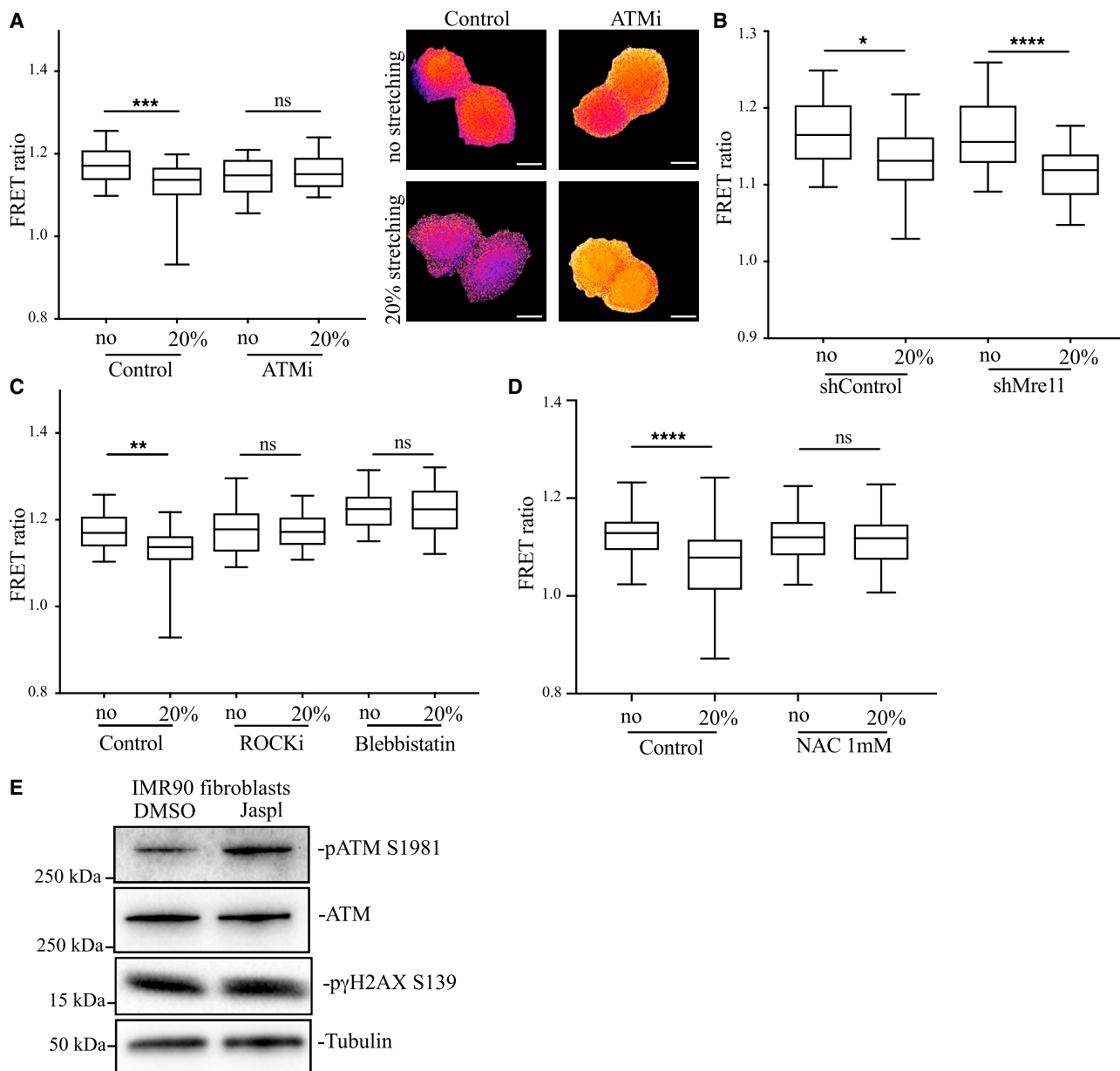
Figure 2. ATM activation following cell stretching is mediated by ROS and does not depend on Mre11

(A) Quantifications and representative images of U2OS cells expressing the WC FRET reporter before and after 20% stretching in presence or absence of ATMi (KU60019, 3 μM) (scale bars, 20 μm). ***p < 0.001, one-way ANOVA test.

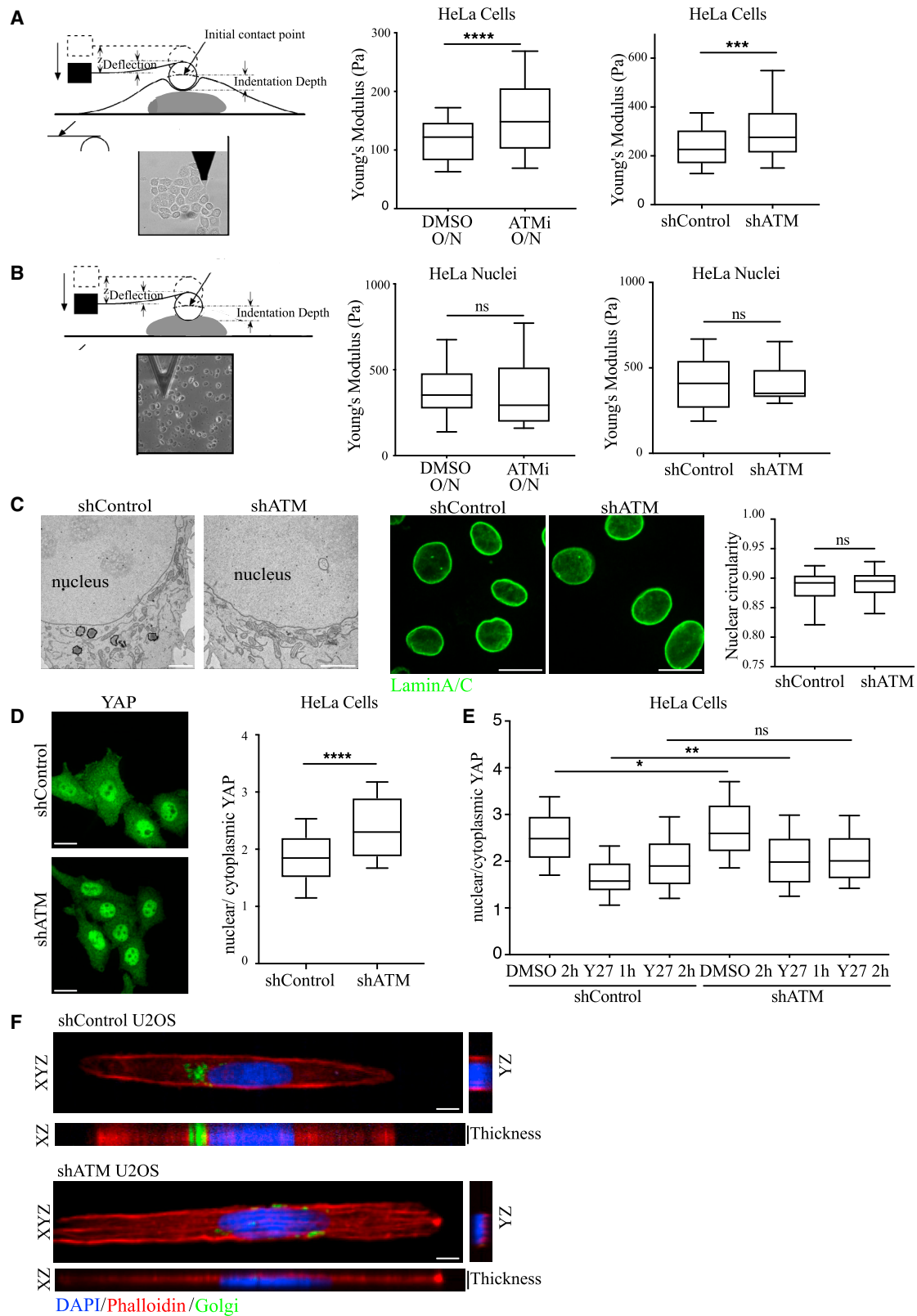(B) ATM activation upon stretching in *MRE11*-depleted cells. *p < 0.05, ****p < 0.0001, one-way ANOVA test.

(C) ATM activation upon stretching following treatments with by ROCKi or Blebbistatin that impair acto-myosin contractility. **p < 0.01, one-way ANOVA test.

(D) ATM activation upon stretching following treatment with the ROS scavenger NAC (1 mM). ****p < 0.0001, one-way ANOVA test.

(E) Western blot showing ATM autophosphorylation at S1981 and γH2AX S139 phosphorylation in IMR90 fibroblasts treated with jasplakinolide (50 nM) for 50 min.

stiffness (Figures 3A and S2A). Mre11 depletion did not affect cell stiffness (Figure S2B). We did not observe changes in nuclear stiffness on isolated ATM-defective nuclei (Figures 3B and S2A). When we analyzed the nuclear morphology using electron microscopy or Lamin A/C staining by immunofluorescence, we failed to observe significant differences between normal cells and ATM-depleted cells (Figures 3C and S2C). The YAP (yes-

associated protein) transcription factor responds to mechanical stress exerted by extracellular matrix or cytoskeletal tension.[58–60] YAP primarily localizes in the cytoplasm when cells are grown on soft substrates, while stiffer environments or high actomyosin contractility trigger YAP nuclear translocation.[60] We found elevation of the YAP nuclear/cytoplasmic ratio in HeLa cells where ATM was depleted with short hairpin RNA

A

HeLa Cells

HeLa Cells

B

HeLa Nuclei

HeLa Nuclei

C

shControl   shATM

shControl   shATM

LaminA/C

Nuclear circularity

D

YAP

shControl

shATM

HeLa Cells

nuclear/ cytoplasmic YAP

E

HeLa Cells

nuclear/cytoplasmic YAP

DMSO 2h Y27 1h Y27 2h DMSO 2h Y27 1h Y27 2h
        shControl   shATM

F

shControl U2OS

XYZ   YZ

XZ   Thickness

shATM U2OS

XYZ   YZ

XZ   Thickness

DAPI/Phalloidin/Golgi

(legend on next page)

(shATM) (Figure 3D), consistent with an increase of cell stiffness. The nuclear localization of YAP in shATM cells was abolished by treating cells with the Rock kinase inhibitor Y-27632 (Figure 3E). The increased cell (but not nuclear) stiffness in ATM-depleted cells may result from cytoskeleton alterations. By staining cells with phalloidin, which recognizes actin stress fibers, we found that ATM depletion resulted in the accumulation of stress fibers (Figure S2D). Since cell shape is influenced by the mechanical properties of the cell and by the cytoskeleton state,[61] we analyzed the role of ATM in coordinating nucleus-cytoskeletal remodeling by imposing a specific shape to the cells. Cells were seeded on 10 μm fibronectin-coated lines (Figures 3F and S2E), forcing them to acquire an elongated shape. ATM depletion caused accumulation of longitudinal and perinuclear actin stress fibers, which also resulted in nuclear flattening (Figures 3F and S2E). We then tested the effect of ATM inhibition on YAP nuclear localization and actin cytoskeleton remodeling upon jasplakinolide treatment in HeLa cells (Figure S2F). Jasplakinolide treatment induced accumulation of actin stress fibers and increased the nuclear fraction of YAP in control cells; ATM inhibition did not influence jasplakinolide-induced YAP nuclear internalization but resulted in a stronger accumulation of actin stress fibers (Figure S2F). Hence, ATM affects the mechanical properties of the cells by influencing the actin cytoskeleton state, and the increased stiffness of ATM-defective cells imposes a mechanical stress on the nuclei, eliciting a YAP-mediated mechano-response.
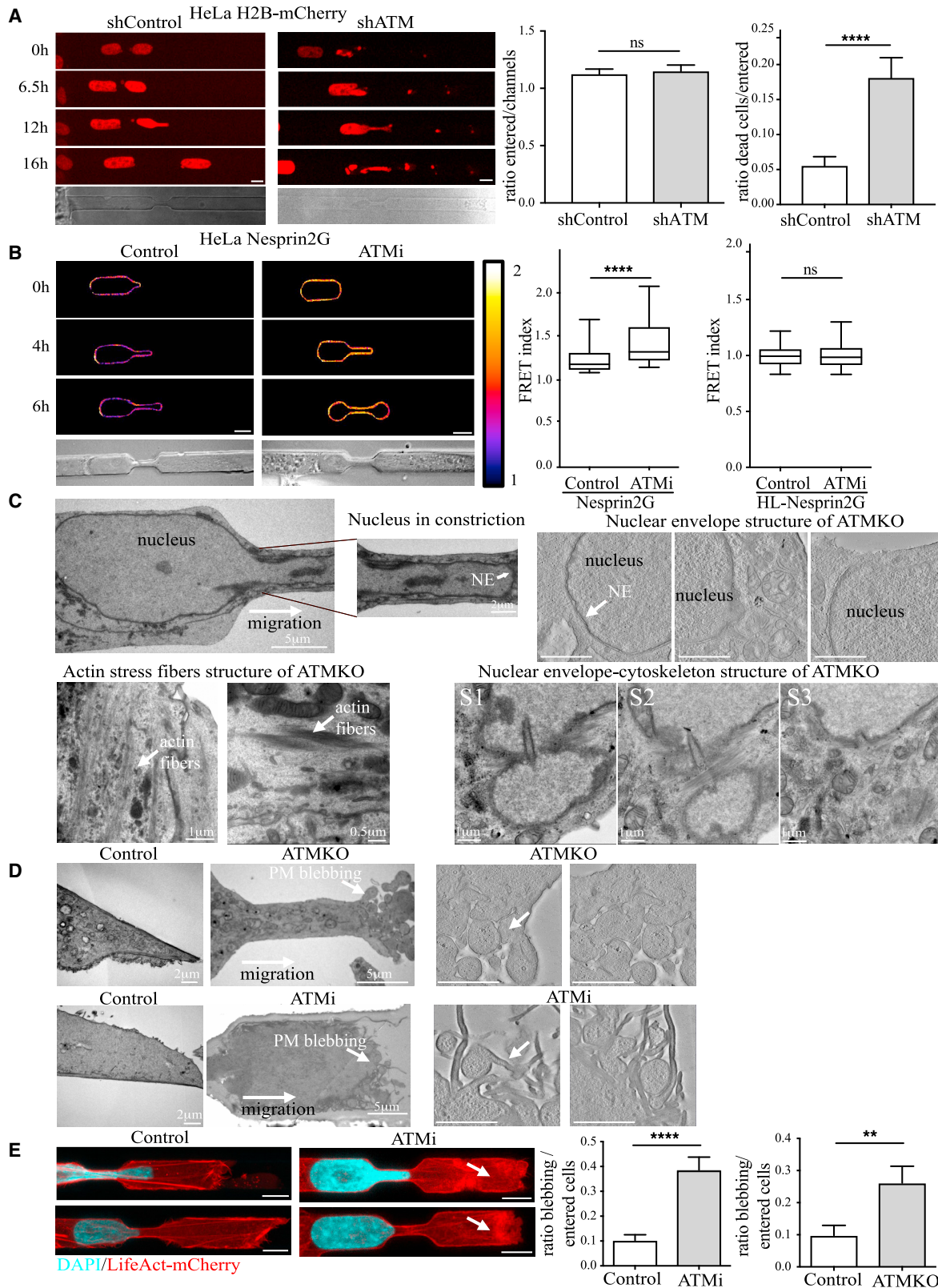
Cell survival during interstitial migration requires ATM

We investigated whether ATM influenced the survival of cells experiencing migration across narrow pores. HeLa cells expressing H2B-mCherry were imaged during interstitial migration. ATM-depleted cells failed to pass through the pores and underwent nuclear fragmentation and cell death (Figure 4A). We obtained analogous results in ATM knockout cells and cells treated with the KU-60019 ATM inhibitor (Figure S3A). ATM inhibition did not affect cell survival when cells migrated across straight channels (Figure S3A) and caused cell death during interstitial migration independently of the cell-cycle stage (Figure S3B). We found that shMre11 HeLa cells behaved like control cells (Figure S3C). Under our experimental conditions, we did not observe any significant changes of 53BP1 foci formation during or after the passage across constrictions (Figure S3D); this is probably due to the difference in pore sizes used for interstitial migration compared to previous published observations.[35,62] The basal level of 53BP1 foci was decreased following ATM inhibition, as

previously published.[63] These results suggest that a non-canonical function of ATM promotes cell survival during interstitial migration. During 3D migration, nuclear passage across narrow pores requires the transmission of mechanical forces between the NE and the cytoskeleton, which largely relies on the LINC (Linker of Nucleoskeleton and Cytoskeleton) complex.[30,42] The NE is subjected to tremendous tension generated by the cytoskeleton on the LINC complex to pull the nucleus across the constrictions.[42,47] We tested whether ATM affects the distance between NE and cytoskeleton using a Nesprin2G FRET sensor[64] that measures the NE-cytoskeleton connection. HeLa cells stably expressing the Nesprin2G sensor were followed during migration with and without ATM inhibition (Figure 4B). ATM-inhibited cells exhibited an increase in the FRET signal along the NE, indicative of a loose connection between the NE and the cytoskeleton in migrating cells. A control experiment using the Nesprin2G headless (HL) control sensor, which cannot be influenced by cytoskeleton forces, showed no alterations in cells treated with the ATM inhibitor (ATMi) (Figure 4B). We then compared the ratio of forces acting in front and at the back of the nuclei migrating inside the channels (Figure S3E). While control cells showed increased tension at the front of the nuclei passing across pores (FRET ratio front/back < 1), ATM inhibition abolished this polar distribution of forces (Figure S3E). We also found that ATM-defective nuclei migrated more slowly than control cells across the constrictions (Figure S3F). Nuclear collapse and cell death in ATM-deficient cells during migration might be caused by compromised mechanical properties of cytoskeleton. We performed electron microscopy (EM) analysis in cells migrating across constrictions to visualize potential structural alterations in cytoplasmic, nuclear, or membrane components (Figure 4C). Previous studies reported occasional ruptures of the NE during nuclear squeezing, which can lead to cell death in membrane repair mutants.[21,29,34] We failed to observe differences at the level of nuclear membranes between control and ATM-depleted cells (Figure 4C). Accordingly, when we monitored the occurrence of NE ruptures following migration across constrictions using a cGAS-GFP reporter that recognizes cytoplasmic DNA leaked from the nucleus,[65,66] we did not find differences between control and ATM-inhibited cells (Figure S3G). We found major alterations of ATM-depleted cells in the cytoplasmic compartment: ATM inhibition/depletion caused accumulation of stress fibers and of plasma membrane blebs at the leading edge (Figures 4C and 4D). The results were confirmed by immunofluorescence of HeLa LifeAct-mCherry cells migrating across constrictions: ATM-depleted cells showed increased plasma

---

Figure 3. ATM regulates cell stiffness independently of nuclear plasticity

(A and B) Schematic representation of the indentation of a cell or an isolated nucleus using a 4.5 μm diameter spherical probe (left) (adapted from Li et al.[54]). Quantifications of AFM measurements performed in HeLa cells or isolated nuclei upon ATMi treatment (KU-60019, 3 μM) or ATM depletion (right). ATM-deficient cells showed increased cell stiffness but no difference in nuclear stiffness. ****p < 0.0001, ***p < 0.001, two-tailed t test.

(C) EM analysis of the NE in shControl and shATM HeLa cells (left) (scale bars, 2 μm). Lamin A/C immunofluorescences of shControl and shATM HeLa cells and relative quantifications of nuclear circularity (right) (scale bars, 20 μm).

(D) Immunofluorescences and quantifications of YAP nuclear/cytoplasmic localization in shATM HeLa cells. ATM-deficient cells showed YAP nuclear accumulation (scale bars, 20 μm). ****p < 0.0001, two-tailed t test.

(E) Quantifications of YAP nuclear/cytoplasmic localization in shControl and shATM HeLa cells treated with the ROCKi Y-27632. ROCKi treatment rescued YAP nuclear localization in shATM HeLa cells. *p < 0.05, **p < 0.01, one-way ANOVA test.

(F) Immunofluorescences of shControl and shATM U2OS cells seeded on 10 μm fibronectin-coated micropattern lines. shATM cells showed increased apical actin stress fibers and nuclear flattening (scale bars, 10 μm).

A HeLa H2B-mCherry

B HeLa Nesprin2G

C Nucleus in constriction

Nuclear envelope structure of ATMKO

Actin stress fibers structure of ATMKO

Nuclear envelope-cytoskeleton structure of ATMKO

D Control | ATMKO | ATMKO

Control | ATMi | ATMi

E Control | ATMi

DAPI/LifeAct-mCherry

(legend on next page)

membrane blebbing and disorganized actin structures at the leading edge of the cell engaged in constrictions, with increased actin stress fibers (Figure 4E). We conclude that ATM-defective cells fail to migrate across constrictions due to cytoskeletal alterations, which affect plasma membrane dynamics and the connections between the LINC complex on the NE and the cytoskeleton.

ATM interacts with F-actin and cytoskeleton factors

We then investigated the potential interaction between ATM and the cytoskeleton. We first performed an immunofluorescence staining of ATM and actin in IMR90 fibroblasts. ATM showed a preferential nuclear localization; however, a fraction of ATM localized in the cytoplasm on actin stress fibers (Figure 5A). We also performed EM analysis of the cellular distribution of ATM using nano-gold labeling and rabbit anti-ATM monoclonal antibody Y170, highly specific for ATM (Figures 5B and S4A). A fraction of cytoplasmic ATM localized on structures morphologically consistent with actin filaments (Figure 5B). Next, we tested biochemically whether ATM interacts with filamentous actin (F-actin). F-actin was added in excess to *Xenopus laevis* egg extracts and pulled down through high-speed centrifugation. We verified by western blotting the presence of cortactin, a protein associated with F-actin (Figure 5C). In the same fraction, we found ATM but not 53BP1. To further investigate the ATM interaction with the cytoskeleton, we performed a proteomic screen with high-resolution mass spectrometry (immunoprecipitation-liquid chromatography-tandem mass spectrometry [IP-LC-MS/MS]). ATM was IPed from exponentially growing HeLa cells using the 9E6 anti-ATM mouse monoclonal antibody. The IP was performed in the presence or absence of DNA damage (Figures S4B and S4C). HeLa ATM knockout (KO) cells were used as control to exclude non-specific bindings (Figure S5B), and ATM interactors were identified using a label-free approach.[67] A significant fraction of the ATM interactome included proteins involved in cytoskeletal regulation (Figure S4C). Many of these proteins were found as putative targets of ATM phosphorylation.[4–6,68,69] We found microtubule components as TUBB, TUBB2B, intermediate filament protein vimentin, factors involved in endocytosis and vesicle trafficking (Rab7a, Rab11A, Rab13, DYNC1H1), and actin cytoskeleton regulators including proteins that regulate acto-myosin contractility through the ROCK pathway and CDC42, such as Rho A, ARHGDIA, and IQGAP1 (Figure S4C). We also found that ATM interacted with several subunits of the Arp2/3 complex (Figure S4C), which forms a perinuclear actin cap required to deform the nucleus during interstitial migration[28]; Arp2/3 inhibition generates plasma membrane blebs during 3D migration,[70] a phenotype also observed in ATM-deficient cells (Figures 4C and 4D). We validated the physical interaction between ATM and Arp3 by IP of GFP-Arp3 in HEK239T cells and by proximity ligation assay (PLA) in HeLa cells (Figures 5D and 5E). Moreover, ATM-deficient cells display phenotypic alterations in filopodia formation during cell spreading, resembling cells treated with Arp2/3 inhibitor (Figure 5F). Altogether, these results suggest that a fraction of ATM interacts with cytoskeleton and cytoskeletal regulators.
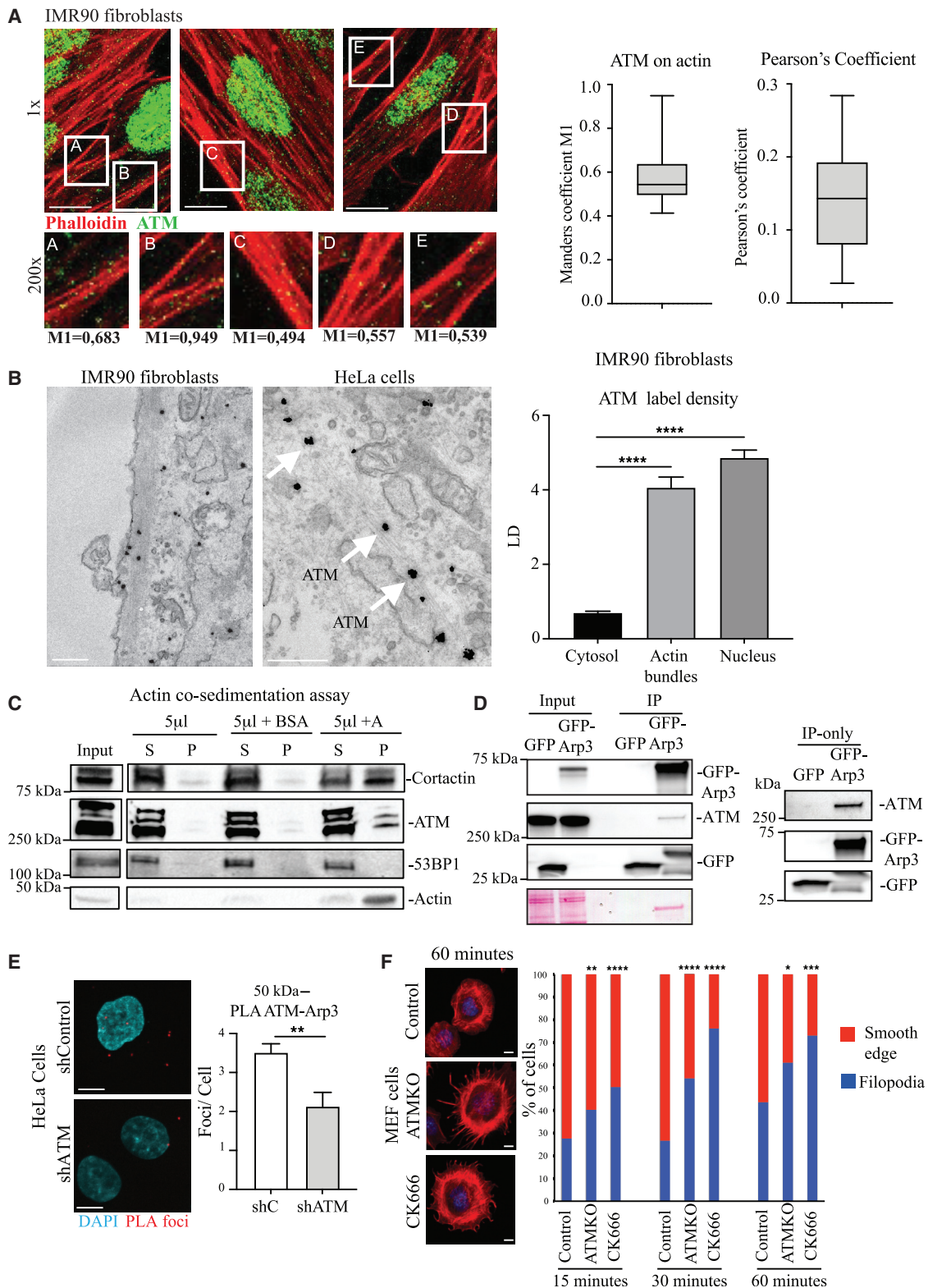
ATM-phosphorylated targets in response to cytoskeleton stress

We performed an MS analysis of IPed proteins with an antibody that specifically binds phosphorylated SQ/TQ motifs, typical of ATM/ATR protein targets.[4] We visualized by EM the cytoskeleton status in IMR90 fibroblasts and found that jasplakinolide treatment caused accumulation of filamentous structures, likely F-actin bundles, as expected (Figure 6A). The IP was performed on IMR90 cells treated without and with jasplakinolide in the presence or absence of the ATMi KU-60019 (Figures 6B and S5A–S5C). 17 proteins were enriched in the sample treated with jasplakinolide, and their enrichment was abolished by treating cells with an ATMi (Figures S5D and S5E) (class I). 23 proteins were enriched specifically in the presence of jasplakinolide and ATMi (class II), implying that their phosphorylation status is counteracted by ATM. Out of these 40 proteins, 12 proteins have SQ/TQ residues (blue), 6 have been shown to be phosphorylated at SQ/TQ motifs (pink), and 15 have been related to phosphorylation events triggered by DNA damage[4,6] (Figure S5D). We also found 7 proteins that do not contain SQ/TQ residues (black circles) (Figure S5D), whose identification might be due to physical interactions with proteins containing SQ/TQ motifs.

In class I, we found proteins involved in chromatin remodeling, RNA metabolism, and cytoskeleton regulation. Among the chromatin remodelers, we found EHMT1, KAT6A, CBX1, and Spin-4. With the exception of Spin-4, they all carry SQ/TQ motifs in their sequence.[4] These proteins regulate the methylation and acetylation status of histone H3. EHMT1 is a histone methyl-transferase that mono- and demethylates lysine 9 and methylates lysine 27 of H3. CBX1(HP1β) binds to methylated lysine 9 of H3 to mediate epigenetic repression and regulates the association of heterochromatin to the inner side of the NE by interaction with the

---

Figure 4. ATM is required for interstitial migration

(A) Survival of shControl and shATM H2B-mCherry HeLa cells migrating through 4 μm constriction channels (scale bars, 10 μm). ****p < 0.0001, two-tailed t test.

(B) HeLa cells expressing the Nesprin2G tension sensor with or without ATMi and relative quantifications. ATM inhibition impairs the cytoskeleton-NE connection (scale bars, 10 μm). ****p < 0.0001, two-tailed t test.

(C) Representative EM image of a control nucleus inside constriction (top left) (scale bars, 5 and 2 μm). EM images of the actin cytoskeleton of ATMKO HeLa cell migrating inside constriction; arrows indicate actin (bottom left) (scale bars, 1 and 0.5 μm). EM analysis of the NE of ATMKO HeLa nuclei inside constrictions showing an intact NE (top right) (scale bars, 5 μm), arrows indicate the NE, and EM showing actin stress fibers deforming the NE (bottom) (scale bars, 1 μm).

(D) EM ultra-structure analysis of the leading edge of control and ATM-depleted cells showing blebbing of the plasma membrane in cells lacking ATM (left) (scale bars, 2 and 5 μm). High-resolution tomography images of the plasma membrane (PM) blebs in cells depleted of ATM (right) (scale bars, 0.5 μm). Arrows indicate PM blebbing.

(E) Immunofluorescence (IF) of control and ATMi-treated HeLa cells migrating inside constrictions stained with DAPI and LifeAct-mCherry. Arrow indicates PM blebbing (left) (scale bars, 10 μm). Quantifications of PM blebbing inside constrictions of live-cell imaging of control and ATM-depleted HeLa LifeAct-mCherry (right). ****p < 0.0001, **p < 0.01, two-tailed t test.

A IMR90 fibroblasts

Phalloidin ATM

A M1=0,683 B M1=0,949 C M1=0,494 D M1=0,557 E M1=0,539

ATM on actin

Pearson's Coefficient

B

IMR90 fibroblasts   HeLa cells

ATM
ATM

IMR90 fibroblasts

ATM label density

C Actin co-sedimentation assay

D

E

HeLa Cells

shControl

shATM

DAPI PLA foci

50 kDa—
PLA ATM–Arp3

F 60 minutes

Control

MEF cells
ATMKO

CK666

Smooth
edge
Filopodia

Lamin B receptor. Spindlin-4 can bind H3K4me3. KAT6A instead acetylates lysine residues of H3 and H4. These 4 chromatin remodelers exhibited interactions with known ATM interactors, including Kap1, which interacts with CBX1 (Figure S5F).

Among I class proteins, we identified DDX5, PRPF4B, STAU1 CCAR1, and HNRNPM, involved in RNA metabolic pathways, myosin1B, TUBB3, leiomodin-1, Zyxin, GRN DENND2A, mediating cytoskeletal remodeling, the RPL26 ribosomal protein, and KPNA1 functioning in nuclear import processes. STRING analysis showed an interaction between CCAR1 and ZYX. In class II, we identified proteins involved in chromatin regulation, stress response, cytoskeleton and RNA metabolism, and cell metabolism.

We then used a custom-made biaxial cell-stretching device that allows proteins extraction and western blot analysis. We subjected IMR90 fibroblasts to continuous 20% cyclic biaxial cell stretching and harvested cells for western blot in a time window between 30 min and 6 h. Analogously to previous observations[71] and to what we showed by immunofluorescence in Figure S1B, we failed to observe a significant increase by western blotting of γH2AX pS139 after up to 6 h of 20% cyclic cell stretching (data not shown). Among the key phosphorylated targets dependent on ATM, we analyzed Kap1[72]; we found that specifically S473, but not S824, was phosphorylated at early time points following cell stretching (30 min) and was dephosphorylated later on at 1.5 h, reaching basal levels in cells stretched for 6 h (Figure 6C). We then analyzed pKAPS473 at shorter time points following cell stretching (5–20 min) in the presence or absence of ATMi and found that pKAPS473 already increased at 5 min following cell stretching and was inhibited by ATMi (Figure 6D). Moreover, treatment of IMR90 fibroblasts with the CHK inhibitor AZD-7762 abolished pKAPS473 under cell stretching (Figure S6A).

CBX1 is known to interact with KAP1, and phosphorylation of KAP1 at S473 modulates their interaction[73,74]; both proteins are involved in regulation of transcription and chromatin methylation status. We depleted CBX1 in HeLa cells and monitored chromatin methylation following 30 min or long-term (6 h) cell stretching. CBX1 depletion resulted in increased H3k27me3 already at 30 min following cell stretching, suggesting that mechanical stress in CBX1-depleted cells generates an altered epigenetic context (Figure 6E). We then analyzed the methylation state of histone H3 following cyclic cell stretching of IMR90 fibroblasts with/without ATMi. Following 6 h cyclic stretching, control cells showed an increase of H3K27me3, as reported,[33,75] and an in-

crease of H3K9me3 (Figure 6F). Altogether, our findings suggest that the ATM-mediated response to mechanical stress coordinates cytoskeleton and chromatin remodeling.

DISCUSSION

ATM coordinates DDR with cell-cycle progression.[76] A-T cells are highly sensitive to radio mimetic drugs. However, A-T is also characterized by metabolic, neurological, and immunological defects,[2,3,77] which cannot be easily ascribed to DDR defects. In recent years, it has become clear that the ATM kinase is regulating a large number nuclear and non-nuclear targets.[4,6,78]

ATM and ATR-mediated responses to mechanical stress
ATM and ATR are PI3 kinases involved in sensing DNA breaks and single-stranded DNA (ssDNA), respectively, and exhibit structural analogies: they contain giant and flexible HEAT domain repeats, ideal to transduce mechanical signals.[16,17] We found that ATR responds to mechanical stress at the NE through a process independent on ssDNA and canonical DDR signaling.[18] This ATR-mediated mechano-transduction pathway maintains nuclear integrity and elasticity and prevents nuclear collapse under conditions causing nuclear compression such as during interstitial migration.[21] Here, we also show that ATM responds to mechanical stress through a process that does not depend on DNA damage and its canonical DDR partner Mre11. The mechano-transduction response that involves ATM differs from the one mediated by ATR at several levels: (1) ATR is activated by nuclear compression and protects NE integrity and nuclear shape, while ATM is activated by cell stretching and acts at the cytoskeleton and chromatin levels; (2) ATM-defective cells are hyper-stiff, while ATR defects cause loss of stiffness, and accordingly, YAP is mostly nuclear when ATM is mutated, while in ATR-defective cells, it accumulates in the cytoplasm; (3) ATM depletion/inhibition causes cytoskeleton abnormalities, while ATR defects lead to NE invaginations and breakage; (4) both ATR- and ATM-defective cells are unable to migrate across constrictions; while ATR-defective cells experience nuclear collapse, ATM-defective cells exhibit nuclear fragmentation as well as cytoskeleton and plasma membrane alterations; and (5) ATR-defective cells elicit the formation of perinuclear cGAS foci following nuclear compression with potential immunological consequences; instead, we failed to observe accumulation of perinuclear cGAS foci in ATM-defective cells

Figure 5. ATM binds to F-actin and cytoskeletal regulators
(A) Immunofluorescences of ATM (green) and actin stained with phalloidin (red) in IMR90 fibroblasts showing partial co-localization of cytoplasmic ATM with actin (scale bars, 10 μm). Graphs show quantifications of Manders' coefficient for ATM on actin and Pearson's coefficient relative to cytoplasmic regions. White boxes highlight regions shown in 200× magnification.
(B) Images of EM sections with enrichment of nano-gold-labeled ATM on actin filaments in IMR90 fibroblasts and HeLa cells; white arrows indicate ATM on actin (left) (scale bars, 0.5 μm). Quantifications of ATM label density (LD) in cytoplasm, actin, and nucleus (right) in IMR90 fibroblasts. ****p < 0.0001, one-way ANOVA test.
(C) F-actin co-sedimentation assay performed in *Xenopus laevis* egg extracts. ATM, but not 53BP1, is enriched in the pellet only in the presence of F-actin. Cortactin: positive control (actin-binding protein).
(D) Validation of ATM-arp3 physical interaction by immunoprecipitation of GFP-Arp3 in HEK293T cells.
(E) Proximity ligation assay (PLA) of ATM and Arp3 in shControl and shATM HeLa cells (scale bars, 10 μm). **p < 0.01, two-tailed t test.
(F) Analysis of filopodia formation during cell spreading of mouse embryonic fibroblast (MEF) control, MEF ATMKO, and MEFs treated with CK-666 50 μM upon PFA 4% fixation at different time points (red: phalloidin staining, blue: DAPI staining) (scale bars, 10 μm). **p < 0.01, ****p < 0.0001, two-tailed t test.
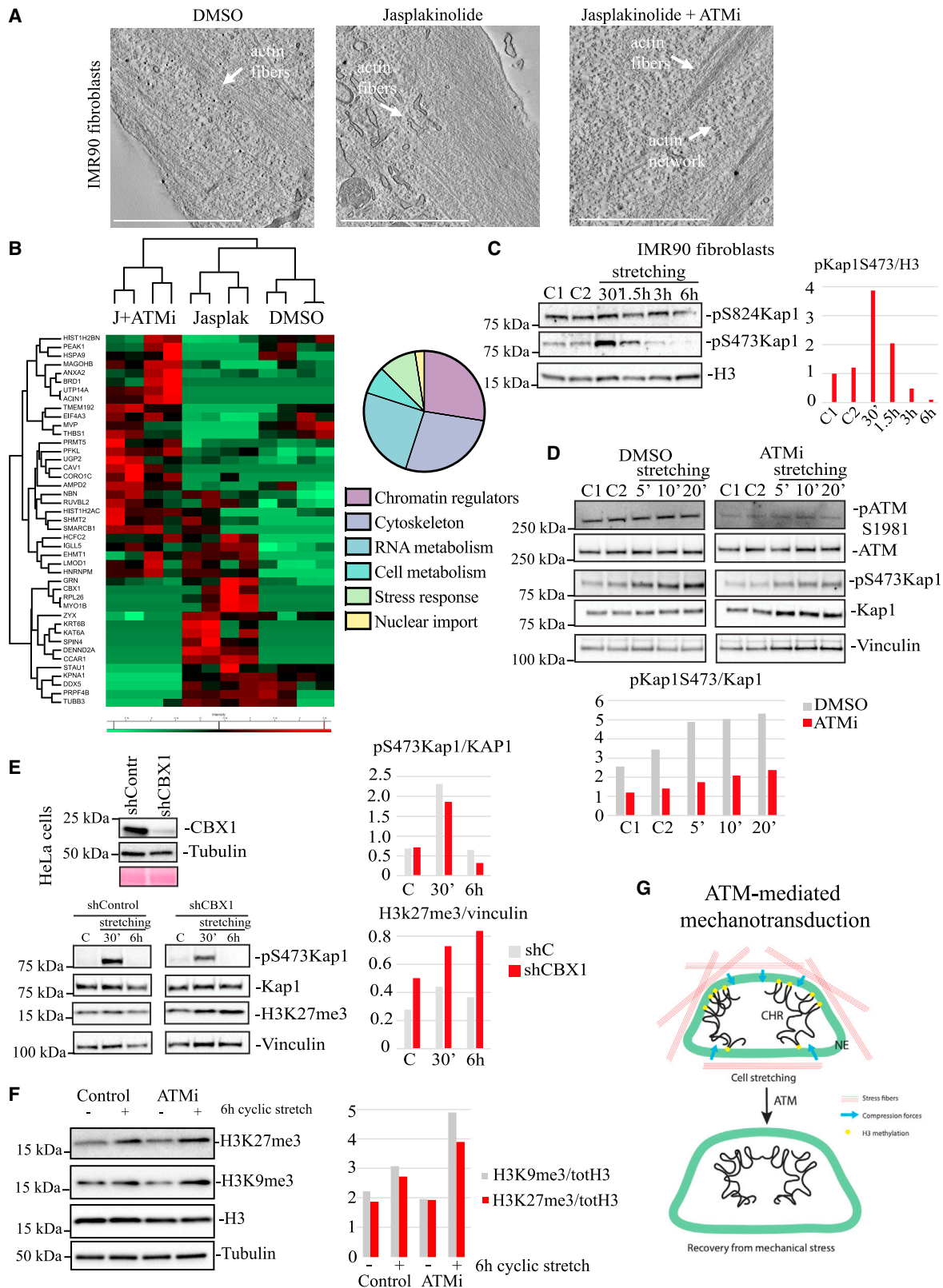
exposed to nuclear mechanical stress. However, in ATM-defective cells, cytoskeleton forces contributing to cell hyper-stiffness likely impose a constitutive stress at the NE level, and under these conditions, cells would have to rely on a functional ATR pathway to prevent the formation of NE invaginations and ruptures. Altogether, our findings point to the existence of an integrated cellular response to mechanical stress in which ATM and ATR have distinct roles unrelated to their canonical DDR functions.

ATM activation following cell stretching

At this stage, we can speculate that ATM activation following cell stretching might be mediated by non-nuclear signals, perhaps generated by cytoskeleton, endoplasmic reticulum (ER) stress, or oxidative stress. Cell stretching leads to important cytoskeletal modifications including actin reorganization around the nucleus.[71] We found that a fraction of ATM colocalizes with actin stress fibers, and therefore it is in the ideal location to sense cytoskeleton changes. We have identified several cytoskeletal proteins that do not represent obvious ATM targets but, on the other hand, may contribute to mediate ATM activation following cytoskeletal stress.

ATM can be activated by ROS levels[12,13] and mediates antioxidant responses.[9,10] Cell stretching generates ER stress and ROS.[52,71,79] Mitochondria, a source of intracellular ROS, physically interact with the cytoskeleton[80]; cell stretching is associated with mitochondrial ruptures and generation of ROS.[52] One possibility is that cell stretching induces ER stress and mitochondrial damage, causing increased ROS levels and activation of cytoskeleton-bound ATM. In this scenario, ROS-mediated ATM activation would then trigger at least two responses by regulating cytoskeleton components but also by shifting the glucose metabolism from glycolysis to the pentose phosphate pathway to initiate an anti-oxidant response.[81] The ROS-mediated ATM regulation following mechanical stress may be part of a larger regulatory circuit involving also the ROS-dependent inhibition of glycolytic enzymes such as PKM2 and GAPDH, coupling the mechano-response to metabolic rewiring of glucose metabolism.[82,83]

ATM-mediated transduction following cell stretching

Nuclear mechanical stress results in epigenetic and transcriptional changes[71,75] and induces alterations at the level H3K9me3 or H3K27me3 that contribute to protect chromosomes from mechanical stress.[33,71] Following cytoskeleton stress, ATM phosphorylates Kap1 and ATM-mediated Kap1 S824 phosphorylation mediates chromatin relaxation to facilitate recruitment of repair factors at DNA damage sites.[84] Therefore, ATM might regulate Kap1 to protect chromatin following mechanical stress. Accordingly, DNA damage causes nuclear softening in an ATM-dependent manner, and ATM inhibition increases H3K9me3 and chromatin compaction.[85,86] We found that jasplakinolide-induced ATM activation causes phosphorylation of EHMT1 and the Kap1 interactor CBX1 and that both proteins methylate H3 and remodel chromatin during mechanical stress.[87,88] The Kap1 S473 site is a target of the ATM-Chk2 axis following DNA damage, and, differently from Kap1 S824, it shows a pan-nuclear decoration.[89–91] Here, we described an early ATM-dependent phosphorylation of Kap1 S473 following mechanical stress. Interestingly, pKap1 S473 was recently identified in a phospho-proteomic analysis as a contraction-regulated phosphorylated site.[92] The pKap1 S473 site regulates its interaction with the chromatin remodeler CBX1, thus suggesting that, following mechanical stress, ATM regulates the KAP1-CBX1 interaction. Accordingly, CBX1 depletion caused chromatin hyper-methylation under cell stretching.

Following cyclic stretching, ATM inhibition results in accumulation of chromatin condensation markers H3K9me3 and H3K27me3. Hp1, Kap1, and PRC2 are key regulators of the H3 methylation state. PRC2, with the methyltransferase EZH2, induces H3K27me3 and acts as a transcriptional repressor.[93] Interestingly, ATM regulates EZH2 protein stability by phosphorylation on Ser734, and lack of ATM was associated with increased PRC2 activity and H3K27me3.[94] Hp1 and Kap1 are both involved in H3K9me3 and can therefore regulate chromatin condensation under mechanical stress. Kap1 binds to Hp1, other methyltransferases, and chromatin remodelers (SUV39H1, SETDP1, and CHD3) to repress transcription by inducing chromatin condensation. We propose that ATM

Figure 6. ATM regulates chromatin condensation during cell stretching and phosphorylates proteins involved in RNA, chromatin and cytoskeletal remodeling following cytoskeletal stress

(A) EM ultra-structural analysis of the actin cytoskeleton in IMR90 fibroblasts treated with DMSO, jasplakinolide, or kasplakinolide+ATMi KU-60019 (3 μM) (scale bars, 0.3 μm). Arrows indicate actin stress fibers.

(B) Heatmap of statistically enriched proteins in jasplakinolide with and without the ATMi KU-60019 following pull-down with anti-pSQ/TQ antibody in IMR90 fibroblasts (MaxQuant analysis of two independent biological replicates). Red: high label-free quantification (LFQ) intensity, green: low LFQ intensity (left). Functional classification of the proteins with statistically relevant changes with/without ATMi identified by mass spectrometry analysis of anti-SQ/TQ pull-down (right).

(C) Western blot showing pKAP1S473 in IMR90 fibroblasts undergoing continuous 20% cyclic biaxial cell stretching using a custom-made cell-stretching device designed for protein lysates preparation. KAP1 is phosphorylated on S473 at 30 min following cell stretching. pKAP1S473/H3 quantifications are shown on the right.

(D) Analysis of induction of pKAP1S473 at short time points post-20% cyclic biaxial cell stretching in IMR90 fibroblasts in presence or absence of ATMi (KU-60019, 10 μM). Inhibitor or DMSO was added 30 min before stretching and maintained during cell stretching. Quantifications of pKAPS473/totKAP1 are shown on the bottom. ATMi prevents pKAP1S473 phosphorylation.

(E) Validation of CBX1 knockdown in HeLa cells by western blot (top). Western blot showing increased H3K27me3 levels in shCBX1 HeLa cells subjected to 20% cyclic biaxial cell stretching for 30 min or 6 h (bottom) and relative quantifications (right).

(F) Western blot showing pKAP S824 and the chromatin condensation markers H3K27me3 and H3K9me3 in IMR90 fibroblasts subjected to biaxial cyclic cell stretching for 6 h in presence and absence of ATMi KU-60019 (top). Quantifications of H3K9me3 and H3K27me3 relative to total H3 showing increased chromatin condensation in cells treated with ATMi and exposed to cyclic stretching (bottom).

(G) Schematic model of ATM-mediated mechano-transduction.

inhibits H3 methylation in the early response to mechanical stress to maintain genome integrity, thus contributing to chromatin relaxation and nuclear softening. ATM could counteract chromatin compaction at different levels: (1) by inhibiting PRC2 activity through Ezh2 phosphorylation and degradation, (2) by direct phosphorylation of hpβ and EHMT1, and (3) by phosphorylation of KAP1 and inhibition of KAP1 binding to H3 methyltransferases.

ATM depletion/inhibition leads to the accumulation of stress fibers and to an aberrant coordination between the nucleus and the cytoskeleton. We identified proteins related to cytoskeletal remodeling that undergo SQ/TQ phosphorylation in an ATM-dependent manner following cytoskeletal stress. In particular, we found that myosin1B, an unconventional myosin, widely expressed in tissues, that functions as a motor protein, localizes to membrane-bound actin filaments[95] and interferes with Arp2/3 complex actin branch filament formations.[96] Myosin1B is influenced by tension forces[97] and counteracts accumulation of actin stress fibers.[98] Leiomodin-1 is an actin filament nucleator,[99] and Zyxin has been implicated in mechano-transduction in regulating actin polymerization at focal adhesion.[100,101]

ATM also phosphorylates proteins involved in RNA metabolism. We note that splicing and RNA export regulatory processes may influence mechano-transduction events at the NE.[102,103]

Based on our data, we speculate that ATM promotes recovery from mechanical stress by phosphorylating a variety of proteins involved in cytoskeleton and chromatin remodeling (Figure 6G).

ATM and interstitial migration

Our data suggest that ATM does not affect directly nuclear integrity during interstitial migration, likely because ATR is active in ATM-defective cells. However, nuclear compression elicits cytoskeleton changes around the nucleus and at the plasma membrane. Our data suggest that the inability of ATM-defective cells to efficiently migrate through pores is due to aberrant cytoskeleton and nuclear coordination. Accordingly, ATM-defective cells experiencing migration across constrictions exhibit massive plasma membrane blebbing and accumulation of perinuclear stress fibers. The Arp2/3 complex generates a perinuclear actin cage when cells enter the constrictions,[28] likely to protect nuclear integrity. Like ATM, Arp2/3 is needed to prevent aberrant plasma membrane blebbing during 3D migration.[70] Our data suggest that ATM might regulate the activity of Arp2/3 during interstitial migration to facilitate nuclear movement across pores.

Limitations of the study

We failed to detect DNA damage in response to mechanical stress. While we cannot rule out that mechanical stress generates DNA damage signals that cannot be detected under our experimental conditions, our data are consistent with other published observations.[71] However, to firmly uncouple the ATM response to mechanical stress from the one induced by DNA damage, it will be crucial to identify the key ATM co-factor(s) that specifically mediate ATM activation following mechanical stress.

STAR★METHODS

Detailed methods are provided in the online version of this paper and include the following:

- KEY RESOURCES TABLE
- RESOURCE AVAILABILITY
  - Lead contact
  - Materials availability
  - Data and code availability
- EXPERIMENTAL MODEL AND STUDY PARTICIPANT DETAILS
- METHOD DETAILS
  - Protein extraction and western blot analysis
  - Protein immunoprecipitation (IP)
  - Mass spectrometry analysis
  - Electron microscopy
  - Cell migration analysis in micro fabricated channels
  - AFM measurements
  - Immunofluorescence analysis
  - Quantification of nuclear morphology and YAP localization
  - Immunofluorescence of actin and nucleus inside micro-channels
  - Cell spreading assay for filopodia formation analysis
  - Proximity ligation assay
  - FRET image acquisition and analysis
  - ATM-FRET analysis upon cell stretching
  - Western blot analysis following cell stretching
  - F-actin co-sedimentation assay in *Xenopus laevis* egg extracts
  - Analysis of cell and nuclear morphology on 10μm-wide line patterns
- QUANTIFICATION AND STATISTICAL ANALYSIS

REFERENCES

1. Shiloh, Y. (2020). The cerebellar degeneration in ataxia-telangiectasia: A case for genome instability. DNA Repair *95*, 102950.

2. Shiloh, Y., and Lederman, H.M. (2017). Ataxia-telangiectasia (A-T): An emerging dimension of premature ageing. Ageing Res. Rev. *33*, 76–88.

3. McKinnon, P.J. (2012). ATM and the molecular pathogenesis of ataxia telangiectasia. Annu. Rev. Pathol. *7*, 303–321.

4. Matsuoka, S., Ballif, B.A., Smogorzewska, A., McDonald, E.R., 3rd, Hurov, K.E., Luo, J., Bakalarski, C.E., Zhao, Z., Solimini, N., Lerenthal, Y., et al. (2007). ATM and ATR substrate analysis reveals extensive pro-tein networks responsive to DNA damage. Science *316*, 1160–1166.

5. Kozlov, S.V., Waardenberg, A.J., Engholm-Keller, K., Arthur, J.W., Gra-ham, M.E., and Lavin, M. (2016). Reactive Oxygen Species (ROS)-Activated ATM-Dependent Phosphorylation of Cytoplasmic Substrates Identified by Large-Scale Phosphoproteomics Screen. Mol. Cell. Prote-omics *15*, 1032–1047.

6. Bensimon, A., Schmidt, A., Ziv, Y., Elkon, R., Wang, S.Y., Chen, D.J., Ae-bersold, R., and Shiloh, Y. (2010). ATM-dependent and -independent dy-namics of the nuclear phosphoproteome after DNA damage. Sci. Signal. *3*, rs3.

7. Li, J., Han, Y.R., Plummer, M.R., and Herrup, K. (2009). Cytoplasmic ATM in neurons modulates synaptic function. Curr. Biol. *19*, 2091–2096.

8. Lim, D.S., Kirsch, D.G., Canman, C.E., Ahn, J.H., Ziv, Y., Newman, L.S., Darnell, R.B., Shiloh, Y., and Kastan, M.B. (1998). ATM binds to beta-adaptin in cytoplasmic vesicles. Proc. Natl. Acad. Sci. USA *95*, 10146–10151.

9. Zhang, J., Tripathi, D.N., Jing, J., Alexander, A., Kim, J., Powell, R.T., Dere, R., Tait-Mulder, J., Lee, J.H., Paull, T.T., et al. (2015). ATM func-tions at the peroxisome to induce pexophagy in response to ROS. Nat. Cell Biol. *17*, 1259–1269.

10. Zhang, Y., Lee, J.H., Paull, T.T., Gehrke, S., D'Alessandro, A., Dou, Q., Gladyshev, V.N., Schroeder, E.A., Steyl, S.K., Christian, B.E., and Shadel, G.S. (2018). Mitochondrial redox sensing by the kinase ATM maintains cellular antioxidant capacity. Sci. Signal. *11*, eaaq0702.

11. Valentin-Vega, Y.A., Maclean, K.H., Tait-Mulder, J., Milasta, S., Steeves, M., Dorsey, F.C., Cleveland, J.L., Green, D.R., and Kastan, M.B. (2012). Mitochondrial dysfunction in ataxia-telangiectasia. Blood *119*, 1490–1500.

12. Guo, Z., Deshpande, R., and Paull, T.T. (2010). ATM activation in the presence of oxidative stress. Cell Cycle *9*, 4805–4811.

13. Guo, Z., Kozlov, S., Lavin, M.F., Person, M.D., and Paull, T.T. (2010). ATM activation by oxidative stress. Science *330*, 517–521.

14. Chen, W.T., Ebelt, N.D., Stracker, T.H., Xhemalce, B., Van Den Berg, C.L., and Miller, K.M. (2015). ATM regulation of IL-8 links oxidative stress to cancer cell migration and invasion. Elife *4*, e07270.

15. Awasthi, P., Foiani, M., and Kumar, A. (2015). ATM and ATR signaling at a glance. J. Cell Sci. *128*, 4255–4262.

16. Grinthal, A., Adamovic, I., Weiner, B., Karplus, M., and Kleckner, N. (2010). PR65, the HEAT-repeat scaffold of phosphatase PP2A, is an elastic connector that links force and catalysis. Proc. Natl. Acad. Sci. USA *107*, 2467–2472.

17. Perry, J., and Kleckner, N. (2003). The ATRs, ATMs, and TORs are giant HEAT repeat proteins. Cell *112*, 151–155.

18. Kumar, A., Mazzanti, M., Mistrik, M., Kosar, M., Beznoussenko, G.V., Mironov, A.A., Garrè, M., Parazzoli, D., Shivashankar, G.V., Scita, G., et al. (2014). ATR mediates a checkpoint at the nuclear envelope in response to mechanical stress. Cell *158*, 633–646.

19. Kidiyoor, G.R., Kumar, A., and Foiani, M. (2016). ATR-mediated regula-tion of nuclear and cellular plasticity. DNA Repair *44*, 143–150.

20. Torres, J., Di Como, C.J., Herrero, E., and De La Torre-Ruiz, M.A. (2002). Regulation of the cell integrity pathway by rapamycin-sensitive TOR function in budding yeast. J. Biol. Chem. *277*, 43495–43504.

21. Kidiyoor, G.R., Li, Q., Bastianello, G., Bruhn, C., Giovannetti, I., Moha-mood, A., Beznoussenko, G.V., Mironov, A., Raab, M., Piel, M., et al. (2020). ATR is essential for preservation of cell mechanics and nuclear integrity during interstitial migration. Nat. Commun. *11*, 4828.

22. Kleckner, N., Zickler, D., Jones, G.H., Dekker, J., Padmore, R., Henle, J., and Hutchinson, J. (2004). A mechanical basis for chromosome function. Proc. Natl. Acad. Sci. USA *101*, 12592–12597.

23. Isermann, P., and Lammerding, J. (2013). Nuclear mechanics and me-chanotransduction in health and disease. Curr. Biol. *23*, R1113–R1121.

24. Zwerger, M., Ho, C.Y., and Lammerding, J. (2011). Nuclear mechanics in disease. Annu. Rev. Biomed. Eng. *13*, 397–428.

25. Denais, C., and Lammerding, J. (2014). Nuclear mechanics in cancer. Adv. Exp. Med. Biol. *773*, 435–470.

26. Rehfeldt, F., Engler, A.J., Eckhardt, A., Ahmed, F., and Discher, D.E. (2007). Cell responses to the mechanochemical microenvironment–im-plications for regenerative medicine and drug delivery. Adv. Drug Deliv. Rev. *59*, 1329–1339.

27. González-Cruz, R.D., Fonseca, V.C., and Darling, E.M. (2012). Cellular mechanical properties reflect the differentiation potential of adipose-derived mesenchymal stem cells. Proc. Natl. Acad. Sci. USA *109*, E1523–E1529.

28. Thiam, H.R., Vargas, P., Carpi, N., Crespo, C.L., Raab, M., Terriac, E., King, M.C., Jacobelli, J., Alberts, A.S., Stradal, T., et al. (2016). Perinu-clear Arp2/3-driven actin polymerization enables nuclear deformation to facilitate cell migration through complex environments. Nat. Commun. *7*, 10997.

29. Denais, C.M., Gilbert, R.M., Isermann, P., McGregor, A.L., te Lindert, M., Weigelin, B., Davidson, P.M., Friedl, P., Wolf, K., and Lammerding, J. (2016). Nuclear envelope rupture and repair during cancer cell migration. Science *352*, 353–358.

30. Friedl, P., Wolf, K., and Lammerding, J. (2011). Nuclear mechanics during cell migration. Curr. Opin. Cell Biol. *23*, 55–64.

31. Nia, H.T., Munn, L.L., and Jain, R.K. (2020). Physical traits of cancer. Sci-ence *370*, eaaz0868.

32. Dahl, K.N., Ribeiro, A.J.S., and Lammerding, J. (2008). Nuclear shape, mechanics, and mechanotransduction. Circ. Res. *102*, 1307–1318.

33. Miroshnikova, Y.A., Nava, M.M., and Wickström, S.A. (2017). Emerging roles of mechanical forces in chromatin regulation. J. Cell Sci. *130*, 2243–2250.

34. Raab, M., Gentili, M., de Belly, H., Thiam, H.R., Vargas, P., Jimenez, A.J., Lautenschlaeger, F., Voituriez, R., Lennon-Duménil, A.M., Manel, N., and Piel, M. (2016). ESCRT III repairs nuclear envelope ruptures during cell migration to limit DNA damage and cell death. Science *352*, 359–362.

35. Xia, Y., Ivanovska, I.L., Zhu, K., Smith, L., Irianto, J., Pfeifer, C.R., Alvey, C.M., Ji, J., Liu, D., Cho, S., et al. (2018). Nuclear rupture at sites of high curvature compromises retention of DNA repair factors. J. Cell Biol. *217*, 3796–3808.

36. Bastianello, G., and Foiani, M. (2023). Mechanisms controlling the mechanical properties of the nuclei. Curr. Opin. Cell Biol. *84*, 102222.

37. Lomakin, A.J., Cattin, C.J., Cuvelier, D., Alraies, Z., Molina, M., Nader, G.P.F., Srivastava, N., Sáez, P.J., Garcia-Arcos, J.M., Zhitnyak, I.Y., et al. (2020). The nucleus acts as a ruler tailoring cell responses to spatial constraints. Science *370*, eaba2894.

38. Venturini, V., Pezzano, F., Català Castro, F., Häkkinen, H.M., Jiménez-Delgado, S., Colomer-Rosell, M., Marro, M., Tolosa-Ramon, Q., Paz-López, S., Valverde, M.A., et al. (2020). The nucleus measures shape changes for cellular proprioception to control dynamic cell behavior. Science *370*, eaba2644.

39. Johnson, S.A., You, Z., and Hunter, T. (2007). Monitoring ATM kinase activity in living cells. DNA Repair *6*, 1277–1284.

40. Montecucco, A., Zanetta, F., and Biamonti, G. (2015). Molecular mechanisms of etoposide. EXCLI J *14*, 95–108.

41. Ghisleni, A., Galli, C., Monzo, P., Ascione, F., Fardin, M.A., Scita, G., Li, Q., Maiuri, P., and Gauthier, N.C. (2020). Complementary mesoscale dynamics of spectrin and acto-myosin shape membrane territories during mechanoresponse. Nat. Commun. *11*, 5108.

42. Liu, L., Luo, Q., Sun, J., and Song, G. (2016). Nucleus and nucleus-cytoskeleton connections in 3D cell migration. Exp. Cell Res. *348*, 56–65.

43. Heuzé, M.L., Collin, O., Terriac, E., Lennon-Duménil, A.M., and Piel, M. (2011). Cell migration in confinement: a micro-channel-based assay. Methods Mol. Biol. *769*, 415–434.

44. Irianto, J., Xia, Y., Pfeifer, C.R., Athirasala, A., Ji, J., Alvey, C., Tewari, M., Bennett, R.R., Harding, S.M., Liu, A.J., et al. (2017). DNA Damage Follows Repair Factor Depletion and Portends Genome Variation in Cancer Cells after Pore Migration. Curr. Biol. *27*, 210–223.

45. Gilbert, H.T.J., Mallikarjun, V., Dobre, O., Jackson, M.R., Pedley, R., Gilmore, A.P., Richardson, S.M., and Swift, J. (2019). Nuclear decoupling is part of a rapid protein-level cellular response to high-intensity mechanical loading. Nat. Commun. *10*, 4149.

46. Khilan, A.A., Al-Maslamani, N.A., and Horn, H.F. (2021). Cell stretchers and the LINC complex in mechanotransduction. Arch. Biochem. Biophys. *702*, 108829.

47. Davidson, P.M., Denais, C., Bakshi, M.C., and Lammerding, J. (2014). Nuclear deformability constitutes a rate-limiting step during cell migration in 3-D environments. Cell. Mol. Bioeng. *7*, 293–306.

48. Stracker, T.H., and Petrini, J.H.J. (2011). The MRE11 complex: starting from the ends. Nat. Rev. Mol. Cell Biol. *12*, 90–103.

49. Chen, C.S. (2008). Mechanotransduction - a field pulling together? J. Cell Sci. *121*, 3285–3292.

50. Pellegrin, S., and Mellor, H. (2007). Actin stress fibres. J. Cell Sci. *120*, 3491–3499.

51. Hotulainen, P., and Lappalainen, P. (2006). Stress fibers are generated by two distinct actin assembly mechanisms in motile cells. J. Cell Biol. *173*, 383–394.

52. Bartolák-Suki, E., Imsirovic, J., Nishibori, Y., Krishnan, R., and Suki, B. (2017). Regulation of Mitochondrial Structure and Dynamics by the Cytoskeleton and Mechanical Factors. Int. J. Mol. Sci. *18*, 1812.

53. Bakkenist, C.J., and Kastan, M.B. (2003). DNA damage activates ATM through intermolecular autophosphorylation and dimer dissociation. Nature *421*, 499–506.

54. Li, Q.S., Lee, G.Y.H., Ong, C.N., and Lim, C.T. (2008). AFM indentation study of breast cancer cells. Biochem. Biophys. Res. Commun. *374*, 609–613.

55. Liu, H., Wen, J., Xiao, Y., Liu, J., Hopyan, S., Radisic, M., Simmons, C.A., and Sun, Y. (2014). In situ mechanical characterization of the cell nucleus by atomic force microscopy. ACS Nano *8*, 3821–3828.

56. Charras, G.T., and Horton, M.A. (2002). Single cell mechanotransduction and its modulation analyzed by atomic force microscope indentation. Biophys. J. *82*, 2970–2981.

57. Trache, A., and Meininger, G.A. (2008). Atomic force microscopy (AFM). Curr Protoc Microbiol *Chapter*. Curr. Protoc. Microbiol. *Chapter 2*. Unit 2C.2.

58. Panciera, T., Azzolin, L., Cordenonsi, M., and Piccolo, S. (2017). Mechanobiology of YAP and TAZ in physiology and disease. Nat. Rev. Mol. Cell Biol. *18*, 758–770.

59. Totaro, A., Castellan, M., Di Biagio, D., and Piccolo, S. (2018). Crosstalk between YAP/TAZ and Notch Signaling. Trends Cell Biol. *28*, 560–573.

60. Dupont, S., Morsut, L., Aragona, M., Enzo, E., Giulitti, S., Cordenonsi, M., Zanconato, F., Le Digabel, J., Forcato, M., Bicciato, S., et al. (2011). Role of YAP/TAZ in mechanotransduction. Nature *474*, 179–183.

61. Théry, M. (2010). Micropatterning as a tool to decipher cell morphogenesis and functions. J. Cell Sci. *123*, 4201–4213.

62. Pfeifer, C.R., Vashisth, M., Xia, Y., and Discher, D.E. (2019). Nuclear failure, DNA damage, and cell cycle disruption after migration through small pores: a brief review. Essays Biochem. *63*, 569–577.

63. Rappold, I., Iwabuchi, K., Date, T., and Chen, J. (2001). Tumor suppressor p53 binding protein 1 (53BP1) is involved in DNA damage-signaling pathways. J. Cell Biol. *153*, 613–620.

64. Arsenovic, P.T., Ramachandran, I., Bathula, K., Zhu, R., Narang, J.D., Noll, N.A., Lemmon, C.A., Gundersen, G.G., and Conway, D.E. (2016). Nesprin-2G, a Component of the Nuclear LINC Complex, Is Subject to Myosin-Dependent Tension. Biophys. J. *110*, 34–43.

65. Sun, L., Wu, J., Du, F., Chen, X., and Chen, Z.J. (2013). Cyclic GMP-AMP synthase is a cytosolic DNA sensor that activates the type I interferon pathway. Science *339*, 786–791.

66. Wu, J., Sun, L., Chen, X., Du, F., Shi, H., Chen, C., and Chen, Z.J. (2013). Cyclic GMP-AMP is an endogenous second messenger in innate immune signaling by cytosolic DNA. Science *339*, 826–830.

67. Lu, P., Vogel, C., Wang, R., Yao, X., and Marcotte, E.M. (2007). Absolute protein expression profiling estimates the relative contributions of transcriptional and translational regulation. Nat. Biotec. *25*, 117–124.

68. Mu, J.J., Wang, Y., Luo, H., Leng, M., Zhang, J., Yang, T., Besusso, D., Jung, S.Y., and Qin, J. (2007). A proteomic analysis of ataxia telangiectasia-mutated (ATM)/ATM-Rad3-related (ATR) substrates identifies the ubiquitin-proteasome system as a regulator for DNA damage checkpoints. J. Biol. Chem. *282*, 17330–17334.

69. Siddoway, B., Hou, H., Yang, H., Petralia, R., and Xia, H. (2014). Synaptic activity bidirectionally regulates a novel sequence-specific S-Q phosphoproteome in neurons. J. Neurochem. *128*, 841–851.

70. Wilson, K., Lewalle, A., Fritzsche, M., Thorogate, R., Duke, T., and Charras, G. (2013). Mechanisms of leading edge protrusion in interstitial migration. Nat. Commun. *4*, 2896.

71. Nava, M.M., Miroshnikova, Y.A., Biggs, L.C., Whitefield, D.B., Metge, F., Boucas, J., Vihinen, H., Jokitalo, E., Li, X., García Arcos, J.M., et al. (2020). Heterochromatin-Driven Nuclear Softening Protects the Genome against Mechanical Stress-Induced Damage. Cell *181*, 800–817.e22.

72. White, D., Rafalska-Metcalf, I.U., Ivanov, A.V., Corsinotti, A., Peng, H., Lee, S.C., Trono, D., Janicki, S.M., and Rauscher, F.J., 3rd. (2012). The ATM substrate KAP1 controls DNA repair in heterochromatin: regulation by HP1 proteins and serine 473/824 phosphorylation. Mol. Cancer Res. *10*, 401–414.

73. Ryan, R.F., Schultz, D.C., Ayyanathan, K., Singh, P.B., Friedman, J.R., Fredericks, W.J., and Rauscher, F.J., 3rd. (1999). KAP-1 corepressor protein interacts and colocalizes with heterochromatic and euchromatic HP1 proteins: a potential role for Kruppel-associated box-zinc finger proteins in heterochromatin-mediated gene silencing. Mol. Cell Biol. *19*, 4366–4378.

74. Chang, C.W., Chou, H.Y., Lin, Y.S., Huang, K.H., Chang, C.J., Hsu, T.C., and Lee, S.C. (2008). Phosphorylation at Ser473 regulates heterochromatin protein 1 binding and corepressor function of TIF1beta/KAP1. BMC Mol. Biol. *9*, 61.

75. Le, H.Q., Ghatak, S., Yeung, C.Y.C., Tellkamp, F., Günschmann, C., Dieterich, C., Yeroslaviz, A., Habermann, B., Pombo, A., Niessen, C.M., and Wickström, S.A. (2016). Mechanical regulation of transcription controls Polycomb-mediated gene silencing during lineage commitment. Nat. Cell Biol. 18, 864–875.

76. Abraham, R.T. (2001). Cell cycle checkpoint signaling through the ATM and ATR kinases. Genes Dev. 15, 2177–2196.

77. Rothblum-Oviatt, C., Wright, J., Lefton-Greif, M.A., McGrath-Morrow, S.A., Crawford, T.O., and Lederman, H.M. (2016). Ataxia telangiectasia: a review. Orphanet J. Rare Dis. 11, 159.

78. Rotman, G., and Shiloh, Y. (1997). Ataxia-telangiectasia: is ATM a sensor of oxidative damage and stress? Bioessays 19, 911–917.

79. Ward, C.W., Prosser, B.L., and Lederer, W.J. (2014). Mechanical stretch-induced activation of ROS/RNS signaling in striated muscle. Antioxidants Redox Signal. 20, 929–936.

80. Moore, A.S., and Holzbaur, E.L.F. (2018). Mitochondrial-cytoskeletal interactions: dynamic associations that facilitate network function and remodeling. Curr. Opin. Physiol. 3, 94–100.

81. Cosentino, C., Grieco, D., and Costanzo, V. (2011). ATM activates the pentose phosphate pathway promoting anti-oxidant defence and DNA repair. EMBO J. 30, 546–555.

82. Anastasiou, D., Poulogiannis, G., Asara, J.M., Boxer, M.B., Jiang, J.K., Shen, M., Bellinger, G., Sasaki, A.T., Locasale, J.W., Auld, D.S., et al. (2011). Inhibition of pyruvate kinase M2 by reactive oxygen species contributes to cellular antioxidant responses. Science 334, 1278–1283.

83. Ralser, M., Wamelink, M.M., Kowald, A., Gerisch, B., Heeren, G., Struys, E.A., Klipp, E., Jakobs, C., Breitenbach, M., Lehrach, H., and Krobitsch, S. (2007). Dynamic rerouting of the carbohydrate flux is key to counteracting oxidative stress. J. Biol. 6, 10.

84. Cheng, C.T., Kuo, C.Y., and Ann, D.K. (2014). KAPtain in charge of multiple missions: Emerging roles of KAP1. World J. Biol. Chem. 5, 308–320.

85. Sherrard, A., Bishop, P., Panagi, M., Villagomez, M.B., Alibhai, D., and Kaidi, A. (2018). Streamlined histone-based fluorescence lifetime imaging microscopy (FLIM) for studying chromatin organisation. Biol. Open 7, bio031476.

86. Dos Santos, Á., Cook, A.W., Gough, R.E., Schilling, M., Olszok, N.A., Brown, I., Wang, L., Aaron, J., Martin-Fernandez, M.L., Rehfeldt, F., and Toseland, C.P. (2021). DNA damage alters nuclear mechanics through chromatin reorganization. Nucleic Acids Res. 49, 340–353.

87. Tajik, A., Zhang, Y., Wei, F., Sun, J., Jia, Q., Zhou, W., Singh, R., Khanna, N., Belmont, A.S., and Wang, N. (2016). Transcription upregulation via force-induced direct stretching of chromatin. Nat. Mater. 15, 1287–1296.

88. Thienpont, B., Aronsen, J.M., Robinson, E.L., Okkenhaug, H., Loche, E., Ferrini, A., Brien, P., Alkass, K., Tomasso, A., Agrawal, A., et al. (2017). The H3K9 dimethyltransferases EHMT1/2 protect against pathological cardiac hypertrophy. J. Clin. Invest. 127, 335–348.

89. Bolderson, E., Savage, K.I., Mahen, R., Pisupati, V., Graham, M.E., Richard, D.J., Robinson, P.J., Venkitaraman, A.R., and Khanna, K.K. (2012). Kruppel-associated Box (KRAB)-associated co-repressor (KAP-1) Ser-473 phosphorylation regulates heterochromatin protein 1beta (HP1-beta) mobilization and DNA repair in heterochromatin. J. Biol. Chem. 287, 28122–28131.

90. Hu, C., Zhang, S., Gao, X., Gao, X., Xu, X., Lv, Y., Zhang, Y., Zhu, Z., Zhang, C., Li, Q., et al. (2012). Roles of Kruppel-associated Box (KRAB)-associated Co-repressor KAP1 Ser-473 Phosphorylation in DNA Damage Response. J. Biol. Chem. 287, 18937–18952.

91. Lee, D.H., Goodarzi, A.A., Adelmant, G.O., Pan, Y., Jeggo, P.A., Marto, J.A., and Chowdhury, D. (2012). Phosphoproteomic analysis reveals that PP4 dephosphorylates KAP-1 impacting the DNA damage response. EMBO J. 31, 2403–2415.

92. Steinert, N.D., Potts, G.K., Wilson, G.M., Klamen, A.M., Lin, K.H., Hermanson, J.B., McNally, R.M., Coon, J.J., and Hornberger, T.A. (2021). Mapping of the contraction-induced phosphoproteome identifies TRIM28 as a significant regulator of skeletal muscle size and function. Cell Rep. 34, 108796.

93. Kadoch, C., Copeland, R.A., and Keilhack, H. (2016). PRC2 and SWI/SNF Chromatin Remodeling Complexes in Health and Disease. Biochemistry 55, 1600–1614.

94. Li, J., Hart, R.P., Mallimo, E.M., Swerdel, M.R., Kusnecov, A.W., and Herrup, K. (2013). EZH2-mediated H3K27 trimethylation mediates neurodegeneration in ataxia-telangiectasia. Nat. Neurosci. 16, 1745–1753.

95. Komaba, S., and Coluccio, L.M. (2010). Localization of myosin 1b to actin protrusions requires phosphoinositide binding. J. Biol. Chem. 285, 27686–27693.

96. Pernier, J., Morchain, A., Caorsi, V., Bertin, A., Bousquet, H., Bassereau, P., and Coudrier, E. (2020). Myosin 1b flattens and prunes branched actin filaments. J. Cell Sci. 133, jcs247403.

97. Laakso, J.M., Lewis, J.H., Shuman, H., and Ostap, E.M. (2008). Myosin I can act as a molecular force sensor. Science 321, 133–136.

98. Makowska, K.A., Hughes, R.E., White, K.J., Wells, C.M., and Peckham, M. (2015). Specific Myosins Control Actin Organization, Cell Morphology, and Migration in Prostate Cancer Cells. Cell Rep. 13, 2118–2125.

99. Chereau, D., Boczkowska, M., Skwarek-Maruszewska, A., Fujiwara, I., Hayes, D.B., Rebowski, G., Lappalainen, P., Pollard, T.D., and Dominguez, R. (2008). Leiomodin is an actin filament nucleator in muscle cells. Science 320, 239–243.

100. Yoshigi, M., Hoffman, L.M., Jensen, C.C., Yost, H.J., and Beckerle, M.C. (2005). Mechanical force mobilizes zyxin from focal adhesions to actin filaments and regulates cytoskeletal reinforcement. J. Cell Biol. 171, 209–215.

101. Hirata, H., Tatsumi, H., and Sokabe, M. (2008). Mechanical forces facilitate actin polymerization at focal adhesions in a zyxin-dependent manner. J. Cell Sci. 121, 2795–2804.

102. Kosar, M., Giannattasio, M., Piccini, D., Maya-Mendoza, A., García-Benítez, F., Bartkova, J., Barroso, S.I., Gaillard, H., Martini, E., Restuccia, U., et al. (2021). The human nucleoporin Tpr protects cells from RNA-mediated replication stress. Nat. Commun. 12, 3937.

103. Bermejo, R., Capra, T., Jossen, R., Colosio, A., Frattini, C., Carotenuto, W., Cocito, A., Doksani, Y., Klein, H., Gómez-González, B., et al. (2011). The replication checkpoint protects fork stability by releasing transcribed genes from nuclear pores. Cell 146, 233–246.

104. Shalem, O., Sanjana, N.E., Hartenian, E., Shi, X., Scott, D.A., Mikkelson, T., Heckl, D., Ebert, B.L., Root, D.E., Doench, J.G., and Zhang, F. (2014). Genome-scale CRISPR-Cas9 knockout screening in human cells. Science 343, 84–87.

105. Lukas, C., Savic, V., Bekker-Jensen, S., Doil, C., Neumann, B., Pedersen, R.S., Grøfte, M., Chan, K.L., Hickson, I.D., Bartek, J., and Lukas, J. (2011). 53BP1 nuclear bodies form around DNA lesions generated by mitotic transmission of chromosomes under replication stress. Nat. Cell Biol. 13, 243–253.

106. Perez-Riverol, Y., Bai, J., Bandla, C., García-Seisdedos, D., Hewapathirana, S., Kamatchinathan, S., Kundu, D.J., Prakash, A., Frericks-Zipper, A., Eisenacher, M., et al. (2022). The PRIDE database resources in 2022: a hub for mass spectrometry-based proteomics evidences. Nucleic Acids Res. 50, D543–D552.

107. Macurek, L., Benada, J., Müllers, E., Halim, V.A., Krejčíková, K., Burdová, K., Pecháčková, S., Hodný, Z., Lindqvist, A., Medema, R.H., and Bartek, J. (2013). Downregulation of Wip1 phosphatase modulates the cellular threshold of DNA damage signaling in mitosis. Cell Cycle 12, 251–262.

108. Shevchenko, A., Wilm, M., Vorm, O., and Mann, M. (1996). Mass spectrometric sequencing of proteins silver-stained polyacrylamide gels. Anal. Chem. 68, 850–858.

109. Rappsilber, J., Mann, M., and Ishihama, Y. (2007). Protocol for micro-purification, enrichment, pre-fractionation and storage of peptides for proteomics using StageTips. Nat. Protoc. 2, 1896–1906.

110. Soffientini, P., and Bachi, A. (2016). STAGE-diging: A novel in-gel digestion processing for proteomics samples. J. Proteonomics *140*, 48–54.

111. Mironov, A.A., Colanzi, A., Polishchuk, R.S., Beznoussenko, G.V., Mironov, A.A., Jr., Fusella, A., Di Tullio, G., Silletta, M.G., Corda, D., De Matteis, M.A., and Luini, A. (2004). Dicumarol, an inhibitor of ADP-ribosylation of CtBP3/BARS, fragments golgi non-compact tubular zones and inhibits intra-golgi transport. Eur. J. Cell Biol. *83*, 263–279.

112. Cutrona, M.B., Beznoussenko, G.V., Fusella, A., Martella, O., Moral, P., and Mironov, A.A. (2013). Silencing of mammalian Sar1 isoforms reveals COPII-independent protein sorting and transport. Traffic *14*, 691–708.

113. Fusella, A., Micaroni, M., Di Giandomenico, D., Mironov, A.A., and Beznoussenko, G.V. (2013). Segregation of the Qb-SNAREs GS27 and GS28 into Golgi vesicles regulates intra-Golgi transport. Traffic *14*, 568–584.

114. Beznoussenko, G.V., Parashuraman, S., Rizzo, R., Polishchuk, R., Martella, O., Di Giandomenico, D., Fusella, A., Spaar, A., Sallese, M., Capestrano, M.G., et al. (2014). Transport of soluble proteins through the Golgi occurs by diffusion via continuities across cisternae. Elife *3*, e02009.

115. Kreft, M.E., Di Giandomenico, D., Beznoussenko, G.V., Resnik, N., Mironov, A.A., and Jezernik, K. (2010). Golgi apparatus fragmentation as a mechanism responsible for uniform delivery of uroplakins to the apical plasma membrane of uroepithelial cells. Biol. Cell. *102*, 593–607.

116. Beznoussenko, G.V., Ragnini-Wilson, A., Wilson, C., and Mironov, A.A. (2016). Three-dimensional and immune electron microscopic analysis of the secretory pathway in Saccharomyces cerevisiae. Histochem. Cell Biol. *146*, 515–527.

117. Lucocq, J.M., Habermann, A., Watt, S., Backer, J.M., Mayhew, T.M., and Griffiths, G. (2004). A rapid method for assessing the distribution of gold labeling on thin sections. J. Histochem. Cytochem. *52*, 991–1000.

118. Mironov, A.A., Jr., and Mironov, A.A. (1998). Estimation of subcellular organelle volume from ultrathin sections through centrioles with a discretized version of the vertical rotator. J. Microsc. *192*, 29–36.

119. Elosegui-Artola, A., Andreu, I., Beedle, A.E.M., Lezamiz, A., Uroz, M., Kosmalska, A.J., Oria, R., Kechagia, J.Z., Rico-Lastres, P., Le Roux, A.L., et al. (2017). Force Triggers YAP Nuclear Entry by Regulating Transport across Nuclear Pores. Cell *171*, 1397–1410.e14.

120. Kardash, E., Bandemer, J., and Raz, E. (2011). Imaging protein activity in live embryos using fluorescence resonance energy transfer biosensors. Nat. Protoc. *6*, 1835–1846.

121. Disanza, A., Carlier, M.F., Stradal, T.E.B., Didry, D., Frittoli, E., Confalonieri, S., Croce, A., Wehland, J., Di Fiore, P.P., and Scita, G. (2004). Eps8 controls actin-based motility by capping the barbed ends of actin filaments. Nat. Cell Biol. *6*, 1180–1188.

122. Pantaloni, D., Boujemaa, R., Didry, D., Gounon, P., and Carlier, M.F. (2000). The Arp2/3 complex branches filament barbed ends: functional antagonism with capping proteins. Nat. Cell Biol. *2*, 385–391.

STAR★METHODS

KEY RESOURCES TABLE

REAGENT or RESOURCE	SOURCE	IDENTIFIER
Antibodies		
anti-ATM [Y170]	abcam	ab32420, RRID:AB_725574
anti-Tubulin	Sigma-Aldrich	T5168, RRID:AB_477579
anti-Nbs1	Cell signaling	3002, RRID:AB_331499
anti-Mre11	Cell signaling	4895, RRID:AB_2145100
anti-phospho ATM (S1981) D25E5	Cell signaling	13050, RRID:AB_2798100
anti-phospoS139 γH2AX	abcam	ab11174, RRID:AB_297813
anti-Lamin A/C 636	Santa Cruz	sc-7292, RRID:AB_627875
anti-YAP 63.7	Santa Cruz	sc-101199, RRID:AB_1131430
anti-phosphoKAp1 S824	Bethyl laboratories	A300-767A, RRID:AB_669740
anti-phosphoKAp1 S824	Cell signaling	4127
anti-CBX1	abcam	ab10478, RRID:AB_297216
anti-phosphoKAP1 S473	Biolegend	654102, RRID:AB_2561782
anti-H3	abcam	Ab1791, RRID:AB_302613
anti-H3K27me3	Cell signaling	9733, RRID:AB_2616029
anti-H3k9me3	abcam	ab8898, RRID:AB_306848
anti-vinculin	Sigma-Aldrich	V9131, RRID:AB_477629
anti-KAP1	ProteinTech	66630-1-IG, RRID:AB_2732886
anti-phospho SQ/TQ	Cell signaling	2851, RRID:AB_330318
Goat anti-Mouse IgG (H + L)-HRP Conjiugate	Bio-Rad	Cat:1706516, RRID: AB_11125547
Goat anti-Rabbit IgG (H + L)-HRP Conjiugate	Bio-Rad	Cat:1706515, RRID: AB_11125542
anti-cortactin	This paper	N/A
anti-53BP1	This paper	N/A
anti-Arp3	This paper	N/A
anti-ATM clone 9E6	This paper	N/A
Anti-GFP mAb magnetic beads clone RQ2	MBL	D153-11
Donkey anti-mouse Alexa Fluor 488	ThermoFisher	A-21202, RRID: AB_141607
Donkey anti-mouse Alexa Fluor 647	ThermoFisher	A-31571, RRID: AB_162542
Donkey anti-mouse Cy3	Jackson Imm Res	715-165-150, RRID: AB_2340813
Donkey anti-rabbit Alexa Fluor 488	ThermoFisher	A-21206, RRID: AB_2535792
Donkey anti-rabbit Alexa Fluor 647	ThermoFisher	A-31573, RRID: AB_2536183
Donkey anti-rabbit Cy3	Jackson ImmunoResearch Labs	715-165-150, RRID: AB_2340813
Chemicals, peptides, and recombinant proteins		
Benzonase	Sigma-Aldrich	E1014
ATMi KU-60019	abcam	ab144817
AZD7762	MedChemExpress	HY-10992
Y-27632	Adooq Biosciences	A11001
Blebbistatin	Sigma-Aldrich	B0560
CK-666 arp2/3 inhibitor	Sigma-Aldrich	SML0006
Jasplakinolide	Sigma-Aldrich	J4580
N-Acetyl Cysteine	Sigma-Aldrich	A7250
Dynabeads™ Protein G	Invitrogen	10004D
Critical commercial assays		
BCA Protein Assay	ThermoFisher	23227
Duolink® *In Situ* Red Starter Kit Mouse/Rabbit	Sigma-Aldrich	DUO92101

(Continued on next page)

Continued

REAGENT or RESOURCE	SOURCE	IDENTIFIER
Alexa Fluor 488 phalloidin	ThermoFisher	A12379
Alexa Fluor 568 phalloidin	ThermoFisher	A12380
DAPI	Sigma-Aldrich	D9542
Fibronectin	Sigma-Aldrich	11080938001
Deposited data		
Mass spectrometry data	PRIDE	PXD032194; https://data.mendeley.com/preview/8zrx4hvw3c?a=4337fb63-f7e8-4022-8ab7-f8a46180b7e3
Experimental models: Cell lines		
HeLa	ATCC	CRM-CCL-2, RRID:CVCL_0030
U2OS	ATCC	HTB-96, RRID:CVCL_0042
IMR90	CORIELL	CVCL_0347, RRID:CVCL_0347
Oligonucleotides		
Cas9 guide forward: ATM1: CACCGCGAATTCGAGTGTGTGAATT	This paper	N/A
Cas9 guide reverse: ATM2: AAACAATTCACACACTCGAATTCGC	This paper	N/A
Recombinant DNA		
H2B-fused ATM FRET reporter	Tony Hunter[39]	N/A
WC ATM FRET reporter	Tony Hunter[39]	N/A
T68A ATM FRET reporter	Tony Hunter[39]	N/A
GFP-Arp3	This paper	N/A
LifeAct-mCherry	This paper	N/A
LentiCRISPR 49535 addgene	Feng Zhang[104]	49535
pLenti6/BLOCK-iT™-DEST	ThermoFisher	K4944-00
pLKO.1-puro	Sigma-Aldrich	SHC001
shCBX1	Sigma-Aldrich	TRCN0000062223
pcDNA nesprin TS addgene	Daniel Conway[64]	68127
pcDNA nesprin HL addgene	Daniel Conway[64]	68128
pTRIP-CMV-GFP-FLAG-cGAS addgene	Matthieu Piel[34]	86675
pAcGFP1-C1	clontech	632470
53BP1-GFP	Jiri Bartek[105]	N/A
Software and algorithms		
PRISM	GraphPad Software	Version 9
Fiji	NIH	https://imagej.net/software/fiji/
ImageJ	NIH	https://imagej.net/ij/
ImageLab Software	Bio-Rad	https://www.bio-rad.com/it-it/product/image-lab-software?ID=KRE6P5E8Z
Other		
INVISISIL™RTV-615 PDMS	Momentive Performance materials	RTV615
Two chambers Lab-TeK II 155379 glasses	ThermoFisher	155379

RESOURCE AVAILABILITY

Lead contact
Further information and requests for resources and reagents should be directed to and will be fulfilled by the lead contact, Marco Foiani (marco.foiani@ifom.eu).

Materials availability
Reagents, protocols and cell lines from this study, are available upon request with a completed Materials Transfer Agreement.

Data and code availability

- The mass spectrometry proteomics data have been deposited to the ProteomeXchange Consortium via the PRIDE partner repository[106] with the dataset identifier PXD032194.
- This paper does not report original code
- Any additional information required to reanalyze the data reported in this work paper is available from the lead contact upon

EXPERIMENTAL MODEL AND STUDY PARTICIPANT DETAILS

HeLa cells and IMR90 fibroblasts were maintained in minimum essential medium with GlutaMAX (MEM; Life Technologies 41090-093) supplemented with 10% (v/v) fetal bovine serum (FBS) South America (SA) (Biowest), 0.1mM NEAA (non-essential amino acids, Microtech), Sodium pyruvate 1mM (Microtech) and penicillin-streptomycin (Microtech). 1% glutamine, 10%FBS SA-DMEM high glucose Lonza 12–614 was used for U2OS cells. Cell culture was performed in 5% CO_2, at 37°C. MEF cells were maintained in 1% glutamine, 10%FBS SA-DMEM high glucose Lonza 12–614 supplemented with 0.1mM NEAA. The Cas9 HeLa control and ATM KO were from Maria Vinciguerra and Vincenzo Costanzo and were generated by cloning the ATM cas9 guide (generated with the ATM1 and ATM2 oligonucleotides) into the Bbs1 site of LentiCRISPR #49535 (Addgene). HeLa cells with stable H2B-mCherry expression were already described.[18] U2OS cells stably expressing 53BP1-GFP cells were from Jiri Bartek.[105] Stable U2OS-FUCCI cells were from Libor Macůrek.[107] Single clones of HeLa stably expressing Nesprin2G or headless sensor were generated in our laboratory[21] as well as stable HeLa LifeAct-mCherry. MEF control and MEF ATMKO were provided by Ylli Doksani.

Lipofectamine2000 (Invitrogen) was used to transfect DNA plasmids into cells. When cells were subjected to lentiviral infection, lentiviral particles were generated by transfection of HEK293T cells with shRNA and viral packaging plasmids; desired cell lines were then infected for 16 h and puromycin or blasticidin were added at 1 μg/ml and 10 μg/ml, respectively, as a selection 48hours after infection. Infected cells were maintained under selection throughout the experiments for a maximum period of 10 days. ATM inhibition was achieved using ATMi KU-60019 3μM.

METHOD DETAILS

Protein extraction and western blot analysis

Cell lysates were prepared in lysis buffer (Tris-HCl pH 8.0 50mM, $MgCl_2$ 1mM, NaCl 200mM, $CaCl_2$ 1mM, Glycerol 10%, NP-40 1%, protease inhibitors (complete inhibitors, Roche), phosphatase inhibitors (phosphatase inhibitor cocktail 2, Sigma or PhosSTOP Merc Life Science), and quantified using the Pierce BCA Protein Assay Kit (Thermo Scientific).

Laemmli buffer was added to the lysates (Tris-HCl pH 6.8 50mM, SDS 2%, Glycerol 10%, βmercaptoethanol 0.1%, Bromophenol blue 0.0005%) and proteins were denatured at 95°C for 10 min. Samples were separated by SDS-page electrophoresis using 4–20% CriterionTGX Biorad or Mini-PROTEAN (Bio-Rad) or NuPAGE (Invitrogen) polyacrylamide precast gels and then transferred on a nitrocellulose membrane for incubation with primary and secondary antibodies. Finally, proteins were visualized with SuperSignal West Dura Extended Duration Substrate (Thermo Scientific) or SuperSignal West Femto Chemiluminescent Substrate (Thermo Scientific). Images were acquired using ChemiDoc (Bio-Rad, Molecular Imager ChemiDoc XRS+) and processed with Imagelab volume tool.

Protein immunoprecipitation (IP)

For the IP of mass spectrometry analysis of ATM physical interactors, HeLa cells were cultured on 10 cm dishes at a confluency of 80% and 10mg of whole protein lysates were used for each sample. Cell lysates were prepared in lysis buffer (TRIS-HCL pH8.0 50mM, $MgCl_2$ 1mM, NaCl 150mM, $CaCl_2$ 1mM, Glycerol 2%, NP-40 0.2%, Benzonase 50U/mL, Protease Inhibitor Roche Tablets 1 for 10mL, phosphatase inhibitor Sigma cocktail 2 1/200) incubated 45 min in ice and centrifuged at maximum speed for 30 min. Lysates were incubated with protein G agarose beads 1 h in rotation in cold room for the pre-clearing then spinned for 10 min at maximum speed at 4°C. Quantification was performed with the Pierce BCA Protein Assay Kit (Thermo Scientific) to adjust to a final concentration of 1 μg/μl 50μL of lysates were stored at −80°C (Input). 10mg of protein lysates were incubated with 60μg of primary antibody (Anti-ATM mouse IgG clone 9E6) and 250μL of protein G dynabeads (Dynabeads Protein G Thermo Fisher Scientific) for 2 h in rotation at 4°C. Following the incubation, 50μL of supernatant were stored at −80°C (flow-through). Samples were washed 3 times for 5 min in rotation at 4°, 50 μL of Laemmli buffer 2X were added to the beads.

Finally samples were boiled 15 min at 95°C and stored at −20°C. Samples were separated by SDS-page electrophoresis on a 4–12% gradient precast gel (Invitrogen) for mass spectrometry analysis.

To pull-down proteins phosphorylated on SQ/TQ motifs we performed the same protocol. Lysates were prepared from IMR90 fibroblasts growing at high confluence on 15 cm Petri dishes, 6 plates were used for each condition. Cells were pre-treated with DMSO or ATMi for 1 h and half, then Jasplakinolide was added at a concentration of 50nM for 50 min in presence or absence of ATMi KU-60019 10μM, DMSO was added as control. Cells were lysed in 1mL of lysis buffer for each 15 cm Petri dishes. Pre-clearing of lysates was performed by incubation with 30 μL of Protein G dynabeads.

IP was performed incubating each sample with 60μL of anti-pSQ/TQ antibody 2851 (Cell Signaling) and 30μL of protein G dynabeads (Dynabeads Protein G Thermo Fisher Scientific) for 1h at 4° in rotation followed by three washes and denaturation in Laemmli buffer as previously described.

Mass spectrometry analysis

The mass spectrometry proteomics data have been deposited to the ProteomeXchange Consortium via the PRIDE partner repository[106] with the dataset identifier PXD032194.

In order to study ATM putative interactors, we analyzed a label free ATM immunoprecipitation by quantitative proteomic approach. We selected the proteins enriched in the IP respect to the control (ATM KO). IP eluates were separated by 4–12% SDS–PAGE (Invitrogen Bolt 4–12% Bis-Tris-Plus), stained with Coomassie Brilliant Blue (Bio-Rad) and excised in three slices for LC-MS/MS analysis. Mass spectrometry analysis was performed by LC-MS/MS using a quadrupole Orbitrap Q-exactive HF mass spectrometer (Thermo Scientific). Each slice was reduced, alkylated and Tryptic digested as described elsewhere.[108] Tryptic digestions were first cleaned using Stage Tips as described previously[109] and then injected into a capillary chromatographic system on a linear gradient from 95% solvent A (2% ACN, 0.1% formic acid) to 55% solvent B (80% acetonitrile, 0.1% formic acid) over 45 min at a constant flow rate of 0.30 μL/min on UHPLC Easy-nLC 1000 (Thermo Scientific) where the LC system was connected to a 23-cm fused-silica emitter of 75 μm inner diameter (New Objective, Inc. Woburn, MA, USA), packed in-house with ReproSil-Pur C18-AQ 1.9 μm beads (Dr Maisch Gmbh, Ammerbuch, Germany) using a high-pressure bomb loader (Proxeon, Odense, Denmark). (EasyLC, Proxeon Biosystems, Odense, Denmark). The mass spectrometer was operated in DDA mode with dynamic exclusion enabled (exclusion duration = 20 s), MS1 resolution = 60,000, MS1 automatic gain control target = 3 x 10^6, MS1 maximum fill time = 20 ms, MS2 resolution = 15,000, MS2 automatic gain control target = 1 x 10^5, MS2 maximum fill time = 80 ms, and MS2 normalized collision energy = 28. For each cycle, one full MS1 scan range = 200–2000 m/z, was followed by 15 MS2 scans using an isolation window size of 1.2 m/z. Protein identification and quantification were achieved using the MaxQuant software version 1.5.2.8. Cysteine carbamidomethylation was searched as a fixed modification, whereas N-acetyl protein and oxidized methionine were searched as variable modifications. Protein quantification was based on extracted ion chromatograms of contained peptides. Peptides and proteins were accepted with a false-discovery rate of 0.01, two minimum peptides identified per protein of which one unique. The experiments were performed using two technical replicates for each biological one.

The mass spectrometry analysis of phosphorylated proteins on SQ/TQ motif following jasplakinolide treatment was performed as follows. Coomassie stained gel lanes were processed according to the STAGE-diging protocol.[110] Briefly, the entire lanes of gel were transferred into the STAGE-diging p1000 tip filled with a double C18 Empore Disk plug (3M, Minneapolis, MN) and submitted to reduction with 10 mM dithiothreitol (DTT), alkylation with 55 mM iodoacetamide (IAA) and digestion by Trypsin o/n at 37°C. Samples were acidified and desalted passing through the C18 plugs and the eluted peptides were dried in a Speed-Vac and resuspended in 5% formic acid.

Each digested sample was analyzed as technical replicate on a UPLC easy-nLC 1200 coupled with a quadrupole Orbitrap Exploris 480 mass spectrometer equipped with a Nanospray Flex ion source and FAIMS operated at −50 and −70 CV (Thermo Fisher Scientific).

Peptides separation was achieved on a linear gradient of 32 min, starting from 95% of solvent A (0.1% formic acid, 2% acetonitrile) and ramping to 50% solvent B (0.1% formic acid), 80% acetonitrile) in 23 min and from 50% to 100% Solvent B in 2 min at a constant flow rate of 0.25 μL min−1. The nLC system was connected to a 25 cm fused-silica emitter of 75 μm inner diameter (New Objective), packed in house with ReproSil-Pur C18-AQ 1.9 μm beads (Dr.Maisch) using a high-pressure bomb loader (Proxeon). MS data were acquired in data-dependent acquisition mode (DDA), with a top15 method for HCD fragmentation. Survey full scan MS spectra (300–1750 Th) were acquired in the Orbitrap with 60,000 resolution, AGC target 1e6, IT 120 m. For HCD spectra the resolution was set to 15,000, AGC target 1e5, IT 120 m; normalized collision energy 28%, isolation width 3.0 m/z with a dynamic exclusion of 5 s.

Raw data were processed with MaxQuant (ver. 1.6.0.16.) using Andromeda search engine, searching against the DataBase uniprot_cp_Human_2020 in which trypsin enzyme was selected with up two missed cleavages. Cysteine carbamidomethylation was used as a fixed modification, methionine oxidation and protein N-terminal acetylation as variable modifications. Mass deviation for MS–MS peaks was set at 20 ppm. The peptide and protein false discovery rates (FDRs) were set to 0.01 with a minimal length for a peptide of seven amino acids; for an high-confidence protein identification a minimum of two peptides and at least one unique peptide were required.

Label-free analysis was carried out, including a 'match between runs' option (time window of 2 min). The lists of identified proteins were filtered to eliminate reverse hits and known contaminants.

Statistical analyses were done using the Perseus program (ver. 1.6.2.3) in the MaxQuant environment, considering the protein LFQ intensity normalized based on the Z score; the function 'imputation' was selected to replace missing values by random numbers drawn from a normal distribution. Supervised Hierarchical Clustering analysis was done applying Anova test and a p value of 0.05.

Electron microscopy

Electron microscopic examination, Immune EM gold-labeling based on pre-embedding, EM tomography and correlative light-electron microscopy (CLEM) were performed as previously described.[18,111–113] A brief description of each process is described below.

Embedding

Cells grown on MatTek dishes (MatTek Corporation, USA) were fixed with of 4% paraformaldehyde and 2.5% glutaraldehyde (EMS, USA) mixture in 0.2 M sodium cacodylate pH 7.2 for 2 h at RT, followed by 6 washes in 0.2 sodium cacodylate pH 7.2 at RT. Then cells were incubated in 1:1 mixture of 2% osmium tetraoxide and 3% potassium ferrocyanide for 1 h at RT followed by 6 times rinsing in cacodylate buffer. Then the samples were sequentially treated with 0.3% Thiocarbohydrazide in 0.2 M cacodylate buffer for 10 min

and 1% OsO4 in 0.2 M cacodylate buffer (pH 6,9) for 30 min. Then, samples were rinsed with 0.1 M sodium cacodylate (pH 6.9) buffer until all traces of the yellow osmium fixative have been removed, washed in de-ionized water, treated with 1% uranyl acetate in water for 1 h and washed in water again.[111,114] The samples were subsequently embedded in Epoxy resin at RT and polymerized for at least 72 h in a 60°C oven. Embedded samples were then sectioned with diamond knife (Diatome, Switzerland) using Leica ultramicrotome. Sections were analyzed with a Tecnai 20 High Voltage EM (FEI, The Netherlands) operating at 200 kV.[113,115]

Nano-gold labeling

Cells grown on MatTeks were fixed with a mixture of 4% paraformaldehyde and 0.05% glutaraldehyde in 0.15M HEPES for 5 min at RT and then replaced with 4% paraformaldehyde in 0.15M HEPES for 30 min. Afterward, the cells were washed 6 times in PBS and incubated with blocking solution for 30 min at RT. Then cells were incubated with primary antibody diluted in blocking solution over-night at 4°C. On the following day, the cells were washed 6 times with PBS and incubated with goat anti-rabbit Fab' fragments coupled to 1.4nm gold particles (diluted in blocking solution 1:100) for 2h and washed 6 times with PBS. Meanwhile, the activated GoldEnhanceTM-EM was prepared according to the manufacturer's instructions and 100 μL were added into each sample well. The reaction was monitored by a conventional light microscope and was stopped after 5–10 min when the cells had turned "dark enough" by washing several times with PBS. Osmification followed: the cells were incubated for 1 h at RT with a 1:1 mixture of 2% osmium tetraoxide in distilled water and 3% potassium ferrocyanide in 0.2 M sodium cacodylate pH 7.4 and then rinsed 6 times with PBS and then with distilled water. The samples were then dehydrated: 3 × 10 min in 50% ethanol; 3 × 10 min in 70% ethanol; 3 × 10 min in 90% ethanol; 3 × 10 min in 100% ethanol. The samples were subsequently incubated for 2h in 1:1 mixture of 100% ethanol and Epoxy resin (Epon) at RT, the mixture was then removed with a pipette and finally samples were embedded for 2 h in Epoxy resin at RT. The resin was polymerized for at least 10 h at 60°C in an oven.[112,113]

Tomography

Two-step CLEM based on the analysis of tomographic reconstructions acquired under low magnification with consecutive reacqui-sition of EM tomo box under high (25000x) magnification and its re-examination was used exactly as described.[116] Briefly, an ultra-tome (LeicaEM 35 UC7; Leica Microsystems, Vienna) was used to cut 60 nm serial thin sections and 200 nm serial semi-thick sec-tions. Sections were collected onto 1% Formvar films adhered to slot grids. Both sides of the grids were labeled with fiduciary 10 nm gold (PAG, CMC, the Netherlands). Tilt series were collected from the samples from ±65° with 1° increments at 200 kV in Tecnai 20 electron microscopes (FEI, Eindhoven. the Netherlands). Tilt series were recorded at a magnification of 11500X, 14500X or 25000X using software supplied with the instrument. The nominal resolution in our tomograms was 4 nm, based upon section thickness, the number of tilts, tilt increments, and tilt angle range. The IMOD package and its newest viewer, 3DMOD 4.0.11, were used to construct individual tomograms. Videos were made in 3DMOD and assembled in QuickTime Pro 7.5 (Apple), and the video size was reduced by saving videos at 480p in QuickTime. CLEM was performed exactly as described.[114]

Quantitation and statistics

The number of ATM-tagged gold particles in different compartments of the cell was counted and percentages were calculated. The labeling density of ATR on different cellular structures was assessed and calculated as described in.[117] For this we used the following criteria: Gold particles were considered to label the NE, ER or mitochondria when these particles were observed over lumens or mem-branes of these compartments; Gold particles were considered as a label of the PM when these particles were observed over the PM. Normality of variant distribution was assessed with Shapiro-Wilk tests. Cumulative probability distributions were compared using the Kolmogorov-Smirnov test. Estimation of the minimal set of samples was performed according to.[118] Correlation between two vari-ables was calculated using Pearson Product Moment Correlation. For analysis of cells in 3D-migration, we embedded PDMS molds on MatTek dishes, cells loaded and incubated for 24 h to facilitate cell migration into the channels. Cells migrating within the channels were examined under the UltraVIEW VoX spinning-disc confocal unit (PerkinElmer), and indicated cells in which the nucleus is either just entering the constriction or is completely in the constriction. We eliminated all the remaining cells from the loading wells and ac-quired images of cells suitable for the future CLEM analysis. 0.05% glutaraldehyde +4% formaldehyde in 0.1 M cacodylate buffer (pH 7.2) was added to the dish for 5 min. Cells were examined again in the microscope and cells with unchanged nuclear position were then fixed with 2.5% glutaraldehyde +4% formaldehyde in 0.2M cacodylate buffer (pH 7.2) for 10 days in order to make cell bodies resistant to the process of the mechanical detachment of PDMS from the MatTek. Then PDMS mold was detached from the MatTek dish and the cells attached to the dishes were processed for EM analysis as described above. After mold detachment, cells were additionally stained with 1% methylene blue in PBS for 3 min at RT and again examined under a light microscope in order to confirm the presence of selected cells on the MatTek glass.

Cell migration analysis in micro fabricated channels

Micro-channels with no constrictions or 15μm-long 4μm-wide constrictions were used in this work. Silicon molds of micro-channels were done in Matthieu Piel's lab and PDMS channels were prepared as previously described.[21,34,43] Briefly, a mixture 1:9 of polymer and crosslinking agent (RTV615 kit) was poured in the silicon mold until complete polymeriation. PDMS channels were bound on 2 chambers Lab-TeK II 155379 glasses (Thermofisher) using plasma treater. Then channels were fibronectin coated overnight, washed with PBS, and filled with cell culture medium for one day (adding treatments or inhibitors when needed). Cells were loaded the day before (for HeLa) or 4 h before the beginning of time-lapse (for U2OS cells). Time-lapse images were acquired (every 15 min, with z-stacks) on an UltraVIEW VoX spinning-disc confocal unit (PerkinElmer), equipped with an Eclipse Ti inverted microscope (Nikon) and a C9100-50 electron-multiplying CCD (charge-coupled device) camera (Hamamatsu), driven by a Volocity software (Improvision;

PerkinElmer). Alternatively, time-lapse images were acquired using an Olympus Spinning Disk CSU based on an Olympus IX83 inverted microscope equipped with an Andor iXon Ultra camera and driven by a CellSens software (Olympus).

A 40X oil immersion and a 20X dry objective were used to acquire images and cells were maintained in an environmental chamber at 37°C in an atmosphere of 5% CO_2. The images were processed using ImageJ and smoothed to reduce the background noise. All the quantifications were performed manually. Fields with no cell migration were discarded from analysis.

Nuclear speed analysis across constrictions was done manually counting the number of frames required for a nucleus to migrate across the pore, only nuclei that performed a complete passage during the time-lapse were considered for the analysis. For cGAS foci analysis, HeLa cells were transiently transfected with cGAS-GFP and loaded in micro-channel device the following day, cells were analyzed during migration as previously described and cGAS-GFP foci were manually counted.

AFM measurements

AFM experiments were performed using Nanowizard 3 (JPK instruments, Germany). For AFM indentation, a modified silicon nitride cantilever (NovaScan, USA) with a spring constant of 0.03N/m and 5μm diameter polystyrene bead adhered to the tip was used to indent the cells. Cells were grown on round glass coverslips that were mounted on the AFM stage and were kept in medium at 37°C using a standard fluid cell and a heater (JPK instruments, Germany) during measurements. Indentation was carried out at the center of cell with a loading rate of 1.5 μm/s. A ramp size of 3 μm and an indentation force of 2 nN were used. All measurements were performed as previously described.[54] To isolate nuclei, cells were rinsed once with PBS and then treated with 1 mL of a 0.01% Igepal CA-630 (a non-ionic detergent, Sigma), 1% citric acid solution in water for 5 min. Expelled nuclei were collected, washed with 5 mL PBS, centrifuged (300g, 5 min), re-suspended in PBS and dropped onto coverslip for AFM experiments.

Immunofluorescence analysis

Cells were seeded on slide-glasses previously coated with Fibronectin 10 μg/ml. The following day cells were washed once with PBS and fixed with 4% formaldehyde (15 min), washed 3 times with PBS (10 min each) then permeabilized with 0.5% Triton X-100 in PBS (5 min), blocked with 3% BSA in 0.1%Triton X-100 PBS for 1 h (blocking buffer), incubated with primary antibodies (diluted in blocking buffer) for minimum 1 h in RT, followed by three PBS washes and then incubated with secondary antibodies (1:400 in blocking solution) for 1 h in dark at RT followed by three PBS washes. DAPI staining was added in PBS for 5 min at RT followed by other 2 washes with PBS. Samples were mounted with Mowiol. Image acquisitions of phalloidin staining, pS139 γH2AX and 53BP1-GFP (on stretching device) were performed using Leica TCS SP2 confocal scanning microscope, equipped with a 63X/1.4NA objective. Single optical sections of the images or maximum projections (step size 0.5 μm or 1 μm) were processed using ImageJ and smoothed to reduce the background noise. The remaining immunofluorescence experiments were acquired on an UltraVIEW VoX spinning-disc confocal unit (PerkinElmer), equipped with a 60X or 40X objective.

Quantification of nuclear morphology and YAP localization

Images from random fields (up to 30) were acquired from coverslips stained with DAPI and Lamin A/C or YAP antibodies using an UltraVIEW VoX spinning-disc confocal unit (PerkinElmer) with a step size of 0.5 μm.

Analysis of nuclear morphology: NE invaginations were analyzed by manual classification of the nuclei showing none, mild and severe invaginations. Circularity index was calculated on central section of Lamin A/C stainings using the ImageJ particle analysis tool and ABsnake plugin.

Analysis of YAP localization was performed as previously described,[119] by measuring the mean intensity of YAP signal in 30pixel diameter regions of interest (ROIs) positioned in the nucleus and in cytoplasm of each cell.

Immunofluorescence of actin and nucleus inside micro-channels

Actin stress fibers and nuclei of HeLa cells migrating inside micro-channels were visualized with LifeAct-mCherry and DAPI staining. DMSO or ATMi 3μM KU-60019 were added in the medium when cell were loaded inside the channels and kept overnight. LifeAct-mCherry HeLa cells migrating inside micro-channels overnight were first washed with PBS then fixed with 4%PFA for 1 h at R/T, washed three times with PBS for 10′ at R/T and permeabilized with 0.5%Triton X-100 PBS for 30 min. DAPI staining in PBS was added for 1 h at R/T, followed by washing with PBS (4 times, for 15 min at R/T). Samples were kept in PBS until imaging acquisition. All procedures were performed keeping cells inside micro-channels.

All images were acquired using a Leica TCS Sp8 confocal microscope equipped with an HC PL APO CS2 63x/1.40 oil objective, maximum projections (step size 0.3μm) were processed using ImageJ.

Cell spreading assay for filopodia formation analysis

MEF control, MEF control treated with Arp2/3 inhibitor CK-666 and MEF ATMKO were analyzed during cell spreading. Cells were trypsinized, counted and re-suspended at a density of 200000 cells/well of 6-well plates. Cells were seeded on slide-glasses 30 min after trypsinization and fixed with PFA 4% 15, 30 and 60 min after seeding. Arp2/3 inhibitor CK-666 50μM was added after trypsinization and left until fixation. IF staining with DAPI and Phalloidin-TRITC was performed with the standard protocol already described. Z-stacks with a step size 0.5 μm from random fields (up to 30) were acquired from coverslips stained with DAPI and Phalloidin-TRITC on an UltraVIEW VoX spinning-disc confocal unit (PerkinElmer) equipped with a 40X objective. The percentage

of cells with lamellipodia or filopodia protrusion during cell spreading were manually counted analyzing the maximum projections of the images collected at three time-points for all conditions.

Proximity ligation assay

The experiment was performed in shControl and shATM HeLa using rabbit polyclonal anti-ATM antibody abcam ab32420 (1:400) and mouse monoclonal anti-Arp3 antibody abcam (1:200), following the protocol from the manufacturer (Sigma, Duolink PLA technology). shATM HeLa cells were used as control for the specificity of the interaction.

FRET image acquisition and analysis

To measure the activity of ATM during interstitial migration, H2B-fused and whole-cell (WC) FRET reporters were used.[39] U2OS cells were transfected with the constructs using Lipofectamine2000 (Invitrogen), 48 h later cells were loaded inside micro-channel, allowed to migrate for 4 h and then analyzed at microscope. The imaging was carried out using a DeltaVision Elite imaging system (Applied Precision) driven by softWoRx software and equipped with a CoolSNAP HQ2 CCD camera (Photometrics) and an environmental chamber (Applied Precision) maintained at 37°C in an atmosphere of 5% CO_2. Images were acquired using an Olympus 60x/1.42 Plan Apo N oil immersion objective. 4 z stacks were acquired for each field of view and cells were imaged every 15 min for 18 h. Three images were collected in sequence at each time point: CFP (ex: 438/24nm, em: 470/24nm), FRET (ex: 438/24nm, em: 559/38nm) and YFP (ex: 513/17nm, em: 528/38nm). Using an in-house macro in ImageJ, images were background corrected, realigned, converted in 32 bits, smoothed and the YFP channel was thresholded and used as a binary mask as described in.[120] The average FRET/CFP ratios calculated for regions of interest were measured at time 0 and at the end of the acquisition in order to compare the FRET efficiency of the reporter in cells migrating inside channels.

The same experimental setup was used for the analysis of FRET ratio before and after 20% uni-axial stretching of HeLa or U2OS cells transfected with the H2B-fused and WC reporters, 30 fields of view were acquired before and after 20% uni-axial stretching.

To measure the tension at the nuclear membrane, HeLa cells stably expressing Nesprin2G or Headless control sensors were generated by Lipofectamine 2000 transfection, Neomycin (G418) selection and single-cell FACS sorting of the mVenus/mTFP1 positive population. These cells were loaded onto the channels in the presence of ATM inhibitor (KU-60019 3μM) or DMSO one day before imaging. Images were acquired with a DeltaVision Elite imaging system using an Olympus 60x/1.42 Plan Apo N oil immersion objective. Three images were collected in sequence at each point: CFP (for mTFP1) (ex: 438/24nm, em: 470/24nm), FRET (ex: 438/24nm, em: 559/38nm) and YFP (for mVenus) (ex: 513/17nm, em: 528/38nm). Single stack images were acquired for each field of view every 2 h for 10h duration. A single plane image was background corrected, realigned, converted into 32 bits and analyzed using an in-house macro in ImageJ. The nuclear membrane of each cell was manually selected as a region of interest (ROI) and average FRET/CFP ratios calculated for the nuclear membrane region. Front/back tension analysis were performed with a custom-made macro as previously described.[21]

ATM-FRET analysis upon cell stretching

Cell stretching experiments were performed using an automated cell-stretching dish (International patent: WO 2018/149795 A1) that can provide uni-axial as well as biaxial stretch with high resolution imaging capability.[41] The components of the cell-stretching dish were designed using SolidWorks software and 3D printed using a stereolithography-based 3D printer (Form 2, Formlabs) coupled with an autoclavable and biocompatible dental resin (Dental SG resin, Formlabs). The printed parts were rinsed in isopropyl alcohol for 5 min to remove any uncured resin from their surface, and then post-cured in a UV box to finalize the polymerization process and stabilize mechanical properties. The printed parts were then polished and assembled to create the lower (cell chamber) and the upper portion (aperture driver) characterizing the stretching dish. Prior to the experiments, the components of the lower portion were autoclaved to be sterilized and assembled to clamp a deformable silicone membrane (thickness 0.005″, SMI), thus creating a cell culture chamber. The dish was coated with fibronectin (10 μg/mL) and incubated at 37°C for 1 h. A total of 10^5 cells were seeded in the cell chamber and incubated overnight. Before starting the imaging, the whole cell-stretching dish was assembled by connecting the upper portion, consisting in the aperture-driving unit, to the cell culture chamber.

20% uni-axial stretching was applied to all the samples under investigation.

HeLa or U2OS cells were transfected with the FRET reporters, the next day cells were seeded on the stretching device at low density and incubated overnight. Finally the device was positioned into a DeltaVision Elite imaging system equipped with an Olympus 60x/1.42 Plan Apo N oil immersion objective. Cells were maintained in an environmental chamber at 37°C. HEPES 25mM was added to the culture medium before starting the acquisition. Fields of view were selected in the central part of the stretching device and cells were imaged once before stretching. An uni-axial stretching of 20% was applied to cells as a single step stretching with no release. Cells were immediately imaged after the stretching selecting fields of view in the central part of the device. At least 30 cells for condition were analyzed for n = 2. Image acquisition and analysis were performed as previously described to measure the FRET signal in cells before and after the stretching.

For the analysis of 53BP1 foci or pS139γH2AX upon cell stretching, HeLa cells or HeLa expressing 53BP1-GFP were seeded on the stretching devices. The next day 0% or 20% uni-axial stretching was applied, then cells were washed with PBS and fixed with 4% paraformaldehyde for 15 min at RT. Standard protocol of immunofluorescence (previously described) was performed on cells seeded on the silicon membrane of the stretching device and images with a Z stacks of 0.5 μm were acquired only in the central area of the

silicon membrane using the Leica TCS SP2 confocal scanning microscope, equipped with a 63X/1.4NA objective previously described. Nuclear ROI were generated using the ImageJ particle analysis tool on DAPI staining and then used to quantify the intensity of 53BP1 or pS139γH2AX signals inside the nucleus at 0% or 20% stretching. 53BP1-GFP foci were counted manually on maximum projections.

Western blot analysis following cell stretching
Western blot analysis following cell stretching was performed using a second custom-made stretching device, whose components were fabricated by the 3D-printing procedure previously described. The device was designed to enclose two flexible membranes (thickness 0.005″, SMI) and membrane stretching was achieved by cyclic aspiration and release of air through a negative and a positive air pump. Following device assembly and sterilization (by rinsing it with 70% EtOH), the upper membrane was coated with fibronectin (10 μg/mL), incubated at 37°C for 1 h and washed three times with 1x PBS sterile. IMR90 fibroblasts were seeded in the cell chamber (200.000/device) and incubated overnight before starting the stretching. Devices were controlled by a MAT pipeline (Fluigent) programmed to exert a 20% cyclic stretch at 0.2 Hz frequency for a total of 6 h inside in a humidified atmosphere (5% CO_2, 37°C). Cells seeded on non-stretched devices were used as control. Following continuous 20% biaxial cyclic cell stretching at different time-points, cells were washed once with 1X PBS, then lysed by adding 150 μL of 2X BOLTLDS buffer complemented with 100 mM DTT and scraping the membrane surface with a cell scraper. Lysates were collected in 1.5 mL tubes on ice, sonicated for 10 s at 4°C then boiled for 10 min at 95°C. Samples were stored at -20°C until ready to be analyzed by Western blot. ATMi (KU60019 10μM) or AZD7762 (500nM) were added 30 min or 1h, respectively, before starting the stretching and maintained until the end of the experiment.

F-actin co-sedimentation assay in *Xenopus laevis* egg extracts
Monomeric rabbit G-actin was induced to polymerize at RT in F-actin buffer (5 mM Tris-HCl, pH 7.8, 0.2 mM ATP, 1 mM DTT, 0.1 mM CaCl2, 1 mM MgCl2 and 100 mM KCl). *Xenopus laevis* egg extracts or control lysis buffer were subsequently incubated with 5μM F-actin in F-buffer 1h at RT. Samples (100 μL) were then loaded over 250 μL of a 30%-glycerol cushion (in F-actin buffer) and ultracentrifuged for 40 min at 100,000xg at 4°C in a Beckman TL-100 table-top ultracentrifuge. Equal amounts of starting materials, supernatants and pellets were solubilized in loading buffer, boiled, and resolved on an SDS–PAGE gel.

Actin was isolated and purified as described.[121,122]

Analysis of cell and nuclear morphology on 10μm-wide line patterns
Bio-adhesive patterns consisting of 10μm-wide adhesive stripes were produced on glass coverslips using deep UV protein micropatterning method. Glass coverslips (24 mm in diameter) were cleaned by sonication in pure Ethanol at RT for 10 min, air-dried, and activated by exposure to air plasma (PDC-32G, Harrick Plasma, Ithaca, NY, USA) for 30sec. Glass slides were then incubated at RT for 1 h with 0.5 mg/ml poly-L-lysine-g-poly(ethyleneglycol) (PLL (20)-g[3.5]-PEG(2); SuSoS Surface Technology, Dubendorf, Switzerland) in 10 mM HEPES at pH 7.5 for passivation, thus creating non-adhesive surface. An additional treatment with 0.2% Pluronic F-127 (Sigma-Aldrich) at RT for 1h was performed to achieve a further passivation. After removal of Pluronic F127, glass slides were rinsed three times with 1× PBS (Phosphate Buffered Saline) and air-dried.

Treated glass slides were then patterned by exposure to deep UV irradiation (UVO Cleaner; Jelight, Irvine, CA, USA) through a synthetic quartz photomask (JD Photo Data, Hitchin, United Kingdom; designed by Paolo Maiuri) for 7min to selectively burn desired PLL-g-PEG/Pluronic F-127 regions, thus creating 10μm-wide adhesive stripes. Patterned glass coverslips were placed in 6-well culture plate, incubated with 10 μg/ml fibronectin in PBS for 1 h at RT, and washed three times with PBS. shControl and shATM HeLa and U2OS cells were seeded on micropatterned glass coverslips at a density of 1x10^4 cells/well and grown at 37°C in a constant 5% CO_2 atmosphere overnight. The next day, cells growing on 10μm-wide lines were stained with DAPI and Phalloidin-TRITC following standard IF protocol to visualize actin stress fibers and nuclei. Random fields (up to 30) were acquired from each coverslip on an UltraVIEW VoX spinning-disc confocal unit (PerkinElmer) equipped with a 40X (U2OS cells) or 60X (HeLa cells) objective. Z-stacks with a step size 0.3μm were acquired for each field of view for a total Z of 8μm. Actin stress fibers were quantified by manual analysis of the Z-stacks images. Cell area was calculated by limiting the measure of the area to the threshold of Phallodin staining with ImageJ.

Nuclear area and nuclear circularity (4pi(area/perimeter^2)) were analyzed using the ImageJ particle analysis tool and shape descriptors on DAPI staining. Nuclear thickness was measured drawing a line equal to the nuclear height on the orthogonal views of the images.

QUANTIFICATION AND STATISTICAL ANALYSIS

The number of replicates and statistical tests used in individual experiments are specified in the figure legends. At least 2 or 3 biological replicates were performed for each experiment. Graphs and relative statistical analyses were carried out using PRISM. Standard deviations or standard errors, in bar graphs, are represented by error bars. Western blots were quantified using the Image lab software (Biorad). Raw files (.scn) were used to allow the quantification of linear and non-saturated signals. Mass spectrometry analyses are described in the corresponding paragraph of the main text and the STAR Methods.